

Modelling of complex interfaces for pendant drop experiments

Citation for published version (APA):

Balemans, C., Hulsen, M. A., & Anderson, P. D. (2016). Modelling of complex interfaces for pendant drop experiments. *Rheologica Acta*, 55(10), 801–822. <https://doi.org/10.1007/s00397-016-0956-1>

DOI:

[10.1007/s00397-016-0956-1](https://doi.org/10.1007/s00397-016-0956-1)

Document status and date:

Published: 01/01/2016

Document Version:

Publisher's PDF, also known as Version of Record (includes final page, issue and volume numbers)

Please check the document version of this publication:

- A submitted manuscript is the version of the article upon submission and before peer-review. There can be important differences between the submitted version and the official published version of record. People interested in the research are advised to contact the author for the final version of the publication, or visit the DOI to the publisher's website.
- The final author version and the galley proof are versions of the publication after peer review.
- The final published version features the final layout of the paper including the volume, issue and page numbers.

[Link to publication](#)

General rights

Copyright and moral rights for the publications made accessible in the public portal are retained by the authors and/or other copyright owners and it is a condition of accessing publications that users recognise and abide by the legal requirements associated with these rights.

- Users may download and print one copy of any publication from the public portal for the purpose of private study or research.
- You may not further distribute the material or use it for any profit-making activity or commercial gain
- You may freely distribute the URL identifying the publication in the public portal.

If the publication is distributed under the terms of Article 25fa of the Dutch Copyright Act, indicated by the "Taverne" license above, please follow below link for the End User Agreement:

www.tue.nl/taverne

Take down policy

If you believe that this document breaches copyright please contact us at:

openaccess@tue.nl

providing details and we will investigate your claim.

Modeling of complex interfaces for pendant drop experiments

Caroline Balemans¹ · Martien A. Hulsen¹ · Patrick D. Anderson¹

Received: 27 January 2016 / Revised: 18 July 2016 / Accepted: 25 July 2016 / Published online: 11 August 2016
© The Author(s) 2016. This article is published with open access at Springerlink.com

Abstract Interfaces of fluid-fluid systems play an important role in the stability of foams and emulsions in chemistry, biology, consumer products, and foods. For most applications, surface active agents are added and adsorbed onto the interface to enhance stability, making the rheological behavior of the interface more complex. To understand the phenomena of these complex interfaces, various techniques are used to determine the interfacial properties. One of the most popular methods is the pendant drop technique. From the equilibrium state of the pendant drop, the interfacial tension of a system can be obtained quite easily in the absence of surface active agents. But when complex viscoelastic interfacial characteristics are considered, in particular in oscillatory measurements, interfacial constitutive relations need to be defined. Interfaces containing proteins, particles or Langmuir monolayers formed by insoluble low weight surfactants appear to act like viscoelastic solid membranes. In this work, a two-dimensional axisymmetric finite element model is designed to study the behavior of complex interfaces in pendant drop experiments. The bulk fluid consists of a Newtonian fluid, while the interface behaves according to the Kelvin-Voigt model as elastic interfacial

forces dominate. To be able to capture large deformations, the Kelvin-Voigt constitutive model is made quasi-linear by using a combination of two non-linear strain tensors. A parameter study is performed to investigate the influence of the five model parameters of the quasi-linear Kelvin-Voigt equation. To demonstrate the applicability of the numerical model, a small amplitude oscillatory measurement is simulated.

Keywords Interface · Numerical · Pendant drop

Introduction

Complex fluid-fluid interfaces are found everywhere among us even though we are not always aware of them. One of the most important characteristics of an interface is the interfacial tension. The interfacial tension is defined as the interfacial free energy per unit area, which is the minimum amount of work required to create or expand the interface by a unit area. The interfacial tension, which can be seen as a material parameter of the fluid-fluid system, is dependent on temperature, but also on miscibility of the components, added particles, or surfactants. The recent review by Fuller and Vermant (2011) summarizes different examples and applications in daily life and industry and outlines the relevance of understanding the dynamics and physics of these complex interfacial transport phenomena. For example, interfacial stabilizers, surfactant molecules, proteins, or particles preferentially residing within the interfacial region are often used to lower the interfacial energy yielding, for example, stability to foams and emulsions, with applications for consumer care products, foods, paints, and other chemical

Electronic supplementary material The online version of this article (doi:10.1007/s00397-016-0956-1) contains supplementary material, which is available to authorized users.

✉ Patrick D. Anderson
p.d.anderson@tue.nl

¹ Polymer Technology, Eindhoven University of Technology, Eindhoven, The Netherlands

products. Furthermore, these systems are found in living organisms as well.

Surface active agents, or “surfactants”, are molecules that can adsorb onto the interface of a fluid-fluid system and alter the interfacial free energy. Rosen (2004) writes that they have a characteristic amphiphathic structure, i.e., a molecular structure containing both a lyophilic group and a lyophobic group. The lyophilic group has strong attraction for the solvent, while the lyophobic group has little attraction for the solvent. At the interface, the surfactants orientate themselves such that the lyophobic groups have minimal contact with the solvent. Usually, this reduces the amount of work required to create or expand the interface and thus decreases the interfacial tension.

Besides classification of surface active agents based on the properties of the hydrophilic group, they can be characterized by the difference in measurable dynamic properties. Roughly, three groups can be distinguished: low molecular weight surfactants, proteins, and particles. The dilatational response dominates the weaker shear phenomena for all three groups. Bos and Van Vliet (2001) concluded that in dilatational rheology, the elasticity is lower if the molecules are present in the solvent as well, compared with insoluble surfactants, because the exchange of molecules between the surface layer and the solvent causes the surfactant layer to behave more viscous. Kotula and Anna (2015) found that the behavior of the interface in the presence of soluble surfactants depends on the surfactant isotherm parameters, transport parameters, and the geometry of the interface. In general, it holds that for more condensed, interacting, or solid-like interfaces, a more explicit viscoelastic response in shear is expected, according to Erni et al. (2012). In particular, the research within the field of interfacial rheology aims at quantifying the mechanical properties of complex fluid-fluid interfaces. More specifically, the relation between deformation and induced stresses is examined.

A variety of experimental techniques are developed to measure several interfacial properties of systems with fluid-fluid interfaces. Most procedures to measure the interfacial tension are based on a thermodynamical equilibrium state. An overview of these methods is given by Drelich et al. (2002). To measure other rheological characteristics of interfacial layers, the techniques are of a more dynamic nature. Derkach et al. (2009) wrote a review on methods of measuring rheological properties of interfacial layers. One technique used for both static and dynamic experiments is the pendant drop method and is widely used to measure the interfacial properties of a system. In particular, the radius of curvature at the apex is the key property of pendant drops together with the droplet volume that is then used to obtain the surface tension (Yeow et al. 2008). During static experiments, the equilibrium state between the surface tension forces and gravitational forces is considered. The dynamic

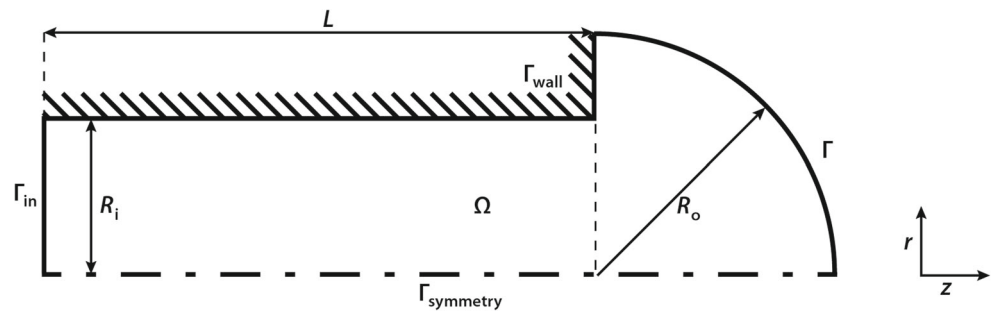
interface characteristics are tested under small amplitude oscillatory conditions. By introducing surface active agents to the system, the interface properties alter, i.e., the behavior of the interface may become more viscoelastic.

To analyze most interfacial rheological experiments, two-dimensional surface constitutive models are used, which are generalized bulk constitutive models. For purely viscous interfaces, the Boussinesq-Scriven model is the two-dimensional analogue of the Newtonian fluid, described by Scriven (1960). On the other hand, for purely elastic interfaces, a generalization of Hooke’s law is often used, as done by Barthès-Biesel and Rallison (1981). Since interfaces with surface active agents behave viscoelastic, constitutive relations like the generalized Maxwell model for interfaces, the Kelvin-Voigt model revised for interfaces, and more elaborate spring-dashpot models can be used to describe these characteristics even more effectively. An extensive review is written by Sagis (2011) on interfacial rheological experiments and the constitutive models used to analyze the behavior of the interfaces.

To computationally describe interfaces and transport on interfaces, different types of models can be used. In particular, the case of highly viscous drops with Newtonian components is studied extensively using the boundary integral model. Research groups of Pozrikis, Zinchenko, and Loewenberg have pioneered the field and demonstrated for a wide variety of flow conditions the complexity introduced by an interface even with a constant interfacial tension (Pozrikidis 1992; Zinchenko and Davis 2006; Zinchenko et al. 1997; Loewenberg and Hinch 1997). Stebe showed by boundary integral modeling that the addition of a surfactant molecule has a large effect on the modes of breakup in extensional flow (Eggleton et al. 2001). Bazhlekov et al. (2006) studied the effect of surfactants on true three-dimensional drop deformation in shear flow, and the authors introduced a morphology diagram that links breakup modes to surfactant coverage. Although boundary integral modeling is very rich and powerful, it is limited to linear systems. Several groups have applied interface capturing techniques that in principle are more general, but they do not provide an explicit description of the interface. Examples are the front capturing work of James and Lowengrub (2004) who developed a surfactant-conserving volume-of-fluid method for interfacial flows with insoluble surfactant. Other approaches are by Voigt and co-workers, and these authors developed a Navier-Stokes-Cahn-Hilliard model for the macroscopic two-phase flow system that is combined with a surface phase-field-crystal model for the microscopic colloidal system along the interface (Aland et al. 2011).

In this work, an axisymmetric finite element interface tracking model is designed to investigate the behavior of complex viscoelastic interfaces for pendant drop experiments.

Fig. 1 Geometry $\Omega_{t=0}$ of the pendant drop, where the outer radius $R_o = 0.35$ mm, the inner radius $R_i = 0.225$ mm, and the length of the capillary $L = 0.8$ mm



Problem description and governing equations

The geometry $\Omega_{t=0}$ of the initial state of the pendant drop is shown in Fig. 1. It is the axisymmetric equivalent of the geometry used in the work of Dieter-Kissling et al. (2014). The axial coordinate is given by z and the radial coordinate by r , using the convention (z, r) . The capillary of the simulation setup is represented by a cylindrical tube with an outer radius of $R_o = 0.35$ mm and an inner radius of $R_i = 0.225$ mm. The length of the capillary is not given in the study of Dieter-Kissling et al. (2014) and is set to $L = 0.8$ mm. The bulk material consists of water with density $\rho = 1000$ kg/m³, dynamic viscosity $\eta = 0.001$ Pa s, and surface tension coefficient $\gamma = 0.072$ N/m. The contact line of the interface Γ is computationally fixed at the outer edge of the capillary.

Balance equations and constitutive model

In this work, an isothermal flow of an incompressible fluid is assumed and the system is described by the following set of equations for the momentum balance and mass balance, respectively,

$$\rho \frac{D\mathbf{u}}{Dt} - \nabla \cdot \boldsymbol{\sigma} = \mathbf{f} \quad \text{in } \Omega \tag{1}$$

$$\nabla \cdot \mathbf{u} = 0 \quad \text{in } \Omega, \tag{2}$$

where ρ is the density, \mathbf{u} the velocity, and \mathbf{f} an external volume force acting on the fluid, which is assumed to be a gravitational force $\mathbf{f} = \rho\mathbf{g}$ applied in z -direction in this work. The Cauchy stress tensor $\boldsymbol{\sigma}$ is defined as

$$\boldsymbol{\sigma} = -p\mathbf{I} + \boldsymbol{\tau}, \tag{3}$$

with pressure p and extra stress tensor $\boldsymbol{\tau}$. It is assumed that the bulk fluid is Newtonian; therefore, the extra stress tensor $\boldsymbol{\tau}$ is given by

$$\boldsymbol{\tau} = 2\eta\mathbf{D}, \tag{4}$$

where $\mathbf{D} = 1/2(\nabla\mathbf{u} + (\nabla\mathbf{u})^T)$ is the symmetric part of the velocity gradient tensor and η is the viscosity. These equations hold in geometry Ω , as shown in Fig. 1.

Boundary, symmetry, and interface conditions

At the inlet of the capillary Γ_{in} , two types of boundary conditions are applied: either a parabolic velocity profile is applied instantaneously by prescribing a certain flow rate Q or a certain pressure p is imposed

$$\mathbf{u} = \mathbf{u}_{prescribed} \quad \text{on } \Gamma_{in} \tag{5}$$

$$\boldsymbol{\sigma} \cdot \mathbf{n} = \mathbf{t}_{prescribed} = -p_{prescribed}\mathbf{n} \quad \text{on } \Gamma_{in}. \tag{6}$$

A no-slip boundary condition is prescribed at the capillary wall Γ_{wall}

$$\mathbf{u} = \mathbf{0} \quad \text{on } \Gamma_{wall}. \tag{7}$$

To imply symmetry, the velocity in radial direction at the symmetry axis $\Gamma_{symmetry}$ is set to zero

$$u_r = 0 \quad \text{on } \Gamma_{symmetry}. \tag{8}$$

The boundary condition at the interface Γ is a Neumann boundary condition

$$\boldsymbol{\sigma} \cdot \mathbf{n} = \nabla_s \cdot \boldsymbol{\zeta} - p_{out}\mathbf{n} \quad \text{on } \Gamma, \tag{9}$$

where ∇_s is the surface gradient operator, $\boldsymbol{\zeta}$ is the interfacial stress tensor, \mathbf{n} is the outwardly directed unit normal vector, and the outside pressure $p_{out} = 0$. The surface gradient operator is defined as $\nabla_s = \mathbf{I}_s \cdot \nabla$ and $\mathbf{I}_s = \mathbf{I} - \mathbf{nn}$ is the second order unit surface dyadic tensor.

Depending on the rheology of the interface, different constitutive models for the interfacial stress tensor $\boldsymbol{\zeta}$ can be used. In the case of linear behavior, a constant interfacial stress can be assumed

$$\boldsymbol{\zeta} = \gamma\mathbf{I}_s, \tag{10}$$

where γ is the static equilibrium value of the interfacial tension. The surface tension γ is kept constant over the interface in time.

For complex interfaces with non-linear behavior, elastic and viscous terms need to be included into the interfacial stress tensor $\boldsymbol{\zeta}$, for example by using a generalized Maxwell model for interfaces or a Kelvin-Voigt interface model. Insoluble low weight surfactants forming Langmuir monolayers, proteins, and particles typically have the response of a viscoelastic solid. The Kelvin-Voigt model is a suitable model for these systems with dominating elasticity and is a

sum of the Boussinesq-Scriven constitutive model for purely viscous fluids (Scriven 1960) and the generalized Hooke's law for purely elastic solids (Barthès-Biesel and Rallison 1981). The model can be made quasi-linear by using a finite strain tensor which can describe the stress response for arbitrary large deformations. Verwijlen et al. (2014) used the Green-Lagrange finite strain tensor $\mathbf{E}_s = 1/2(\mathbf{C}_s - \mathbf{I}_s)$ for one formulation of the quasi-linear two-dimensional Kelvin-Voigt model and the Hencky strain tensor $\mathbf{H}_s = 1/2 \ln(\mathbf{C}_s)$ for a second formulation. Herein, $\mathbf{C}_s = \mathbf{F}_s^T \cdot \mathbf{F}_s$ is the Cauchy-Green deformation tensor of the interface with $\mathbf{F}_s = (\nabla_{s,0}\mathbf{x}_\Gamma)^T$ is the surface deformation gradient tensor, expressing the deformation of a certain material point \mathbf{x}_Γ on the interface with respect to the initial undeformed state, indicated by subscript 0. From application of these two formulations of the model to both pure dilatation and simple shear, the formulation using the Hencky strain tensor appears to be more appropriate for dilatational deformation, whereas the formulation using the Green-Lagrange strain tensor is more suitable for shear deformation. In both formulations, the shear and dilatational contributions are separated. Combining the dilatational contribution using the Hencky strain tensor with the shear contribution using the Green-Lagrange strain tensor, the quasi-linear two-dimensional Kelvin-Voigt viscoelastic constitutive equation becomes

$$\boldsymbol{\zeta} = \gamma \mathbf{I}_s + \kappa (\nabla_s \cdot \mathbf{u}) \mathbf{I}_s + \mu \left[\nabla_s \mathbf{u} + (\nabla_s \mathbf{u})^T - (\nabla_s \cdot \mathbf{u}) \mathbf{I}_s \right] + K \ln(J^{1/2}) \mathbf{I}_s + G (J^{-1/2} \mathbf{C}_s - \mathbf{I}_s) \quad (11)$$

Herein, κ is the surface dilatational viscosity, μ the surface shear viscosity, K the surface dilatational elasticity, G the surface shear elasticity, and $J = \det(\mathbf{C}_s)$. Furthermore, $J^{1/2}$ represents the change in interfacial area A/A_0 .

Particle laden interfaces may exhibit bending moduli that are not marginal, as shown by Yunker et al. (2012). These bending stresses arise when the thickness of the interface is nonzero. In this work, however, the influence of bending stresses is assumed to be negligible compared to the surface tension, dilatational, and shear stresses. Therefore, the interfaces are modeled with a zero thickness.

If a complex interface is assumed, the quasi-linear Kelvin-Voigt model of Eq. (11) is prescribed to the interface. The value of the surface tension γ may be different from the value of pure water. All parameters of the viscoelastic interface are constants. Furthermore, other interfacial dynamics like Marangoni flows at the interface and diffusion of material between the bulk and the interface are neglected.

Evolution of the pendant drop in time

The motion of the interface Γ is determined using a FEM-based interface tracking method. A moving curvilinear coordinate system describes the interface according to

$$\mathbf{x}_\Gamma = \mathbf{x}_\Gamma(\underline{\xi}, t), \quad (12)$$

where \mathbf{x}_Γ is the function that maps the curvilinear coordinates $\underline{\xi} = (\xi^1, \xi^2)$ onto the spatial coordinates \mathbf{x}_Γ of the interface. The interface is tracked in a Lagrangian way. Therefore, the velocity of the interface is defined as

$$\frac{d\mathbf{x}_\Gamma}{dt} = \mathbf{u}. \quad (13)$$

Herein, \mathbf{u} is the material velocity at the interface.

Surface strain

To quantify the deformation of the interface, the strain is calculated in tangential and circumferential direction, using the stretch ratio of the interface. The stretch ratio in the tangential direction is given by

$$\lambda_t = \sqrt{\mathbf{t} \cdot (\mathbf{F}_s \cdot \mathbf{F}_s^T) \cdot \mathbf{t}}. \quad (14)$$

Herein, \mathbf{t} is the unit tangential vector.

The stretch ratio in circumferential direction is determined by

$$\lambda_c = \sqrt{\mathbf{e}_{\theta\theta} \cdot (\mathbf{F}_s \cdot \mathbf{F}_s^T) \cdot \mathbf{e}_{\theta\theta}} = \frac{r}{r_0}, \quad (15)$$

where $\mathbf{e}_{\theta\theta}$ is the unit vector in circumferential direction, r is the current radius, and r_0 is the initial radius of the interface, respectively.

The stretch ratios are used to calculate the linear strain, defined as

$$\varepsilon = \lambda - 1 \quad (16)$$

both in tangential and circumferential direction.

Numerical method

Weak form

As stated in the introduction, the finite element method is applied to solve the governing equations with appropriate boundary conditions as discussed in the previous section. In order to derive the weak form, the momentum balance and

mass balance are multiplied with the test functions \mathbf{v} and q in the appropriate function spaces

$$\left(\mathbf{v}, \rho \frac{D\mathbf{u}}{Dt} - \nabla \cdot \boldsymbol{\sigma} \right) = (\mathbf{v}, \mathbf{f}) \quad \text{on } \Omega \tag{17}$$

$$(q, \nabla \cdot \mathbf{u}) = 0 \quad \text{on } \Omega. \tag{18}$$

Note that (\cdot, \cdot) defines the inner product on Ω in the usual manner by

$$(a, c) = \int_{\Omega} ac \, dV, \quad (\mathbf{a}, \mathbf{c}) = \int_{\Omega} \mathbf{a} \cdot \mathbf{c} \, dV, \tag{19}$$

$$(\mathbf{A}, \mathbf{C}) = \int_{\Omega} \mathbf{A} : \mathbf{C} \, dV$$

for scalars a and c , vectors \mathbf{a} and \mathbf{c} , and tensors \mathbf{A} and \mathbf{C} . For a tensor \mathbf{A} and vector \mathbf{a} , the product rule holds

$$\nabla_s \cdot (\mathbf{A} \cdot \mathbf{a}) = \mathbf{a} \cdot (\nabla_s \cdot \mathbf{A}) + (\nabla_s \mathbf{a})^T : \mathbf{A} \tag{20}$$

and the surface divergence theorem, as described by Weatherburn (1955), is given by

$$\int_{\Gamma} \nabla_s \cdot \mathbf{a} \, dS = \int_{\Gamma} (\nabla_s \cdot \mathbf{n}) \mathbf{n} \cdot \mathbf{a} \, dS + \oint_{\partial\Gamma} \mathbf{b} \cdot \mathbf{a} \, ds, \tag{21}$$

where $\mathbf{b} = \mathbf{t} \times \mathbf{n}$ is the binormal and $\partial\Gamma$ the boundary of the interface. In our geometry, the boundary of the interface $\partial\Gamma$ is the connection of interface Γ to the capillary wall Γ_{wall} . Using these two theorems, the boundary condition on the interface in the weak formulation can be written as

$$\begin{aligned} \int_{\Gamma} \mathbf{v} \cdot (\boldsymbol{\sigma} \cdot \mathbf{n}) \, dS &= \int_{\Gamma} \mathbf{v} \cdot (\nabla_s \cdot \boldsymbol{\zeta}) \, dS \\ &= - \int_{\Gamma} (\nabla_s \mathbf{v})^T : \boldsymbol{\zeta} \, dS + \int_{\Gamma} \nabla_s \cdot (\boldsymbol{\zeta} \cdot \mathbf{v}) \, dS \\ &= - \int_{\Gamma} (\nabla_s \mathbf{v})^T : \boldsymbol{\zeta} \, dS + \int_{\Gamma} (\nabla_s \cdot \mathbf{n}) \mathbf{n} \cdot (\boldsymbol{\zeta} \cdot \mathbf{v}) \, dS \\ &\quad + \oint_{\partial\Gamma} \mathbf{b} \cdot (\boldsymbol{\zeta} \cdot \mathbf{v}) \, ds. \end{aligned} \tag{22}$$

The interfacial stress tensor $\boldsymbol{\zeta}$ is always tangential to the surface, as a result of which $\mathbf{n} \cdot \boldsymbol{\zeta} = 0$ and the second term of the right hand side is zero.

The complete weak form including the boundary terms becomes: Find \mathbf{u} and p such that

$$\begin{aligned} \left(\mathbf{v}, \rho \left(\frac{\partial \mathbf{u}}{\partial t} + \mathbf{u} \cdot \nabla \mathbf{u} \right) \right. \\ \left. + (\mathbf{D}_v, 2\eta \mathbf{D}) \right. \\ \left. - (\nabla \cdot \mathbf{v}, p) \right) = - \left((\nabla_s \mathbf{v})^T, \boldsymbol{\zeta} \right)_{\Gamma} \\ + (\mathbf{b}, \boldsymbol{\zeta} \cdot \mathbf{v})_{\partial\Gamma} \\ + (\mathbf{v}, \rho \mathbf{g}) \end{aligned} \quad \text{on } \Omega \tag{23}$$

$$(q, \nabla \cdot \mathbf{u}) = 0 \quad \text{on } \Omega \tag{24}$$

for all possible test functions \mathbf{v} and q and where $\mathbf{D}_v = 1/2 (\nabla \mathbf{v} + (\nabla \mathbf{v})^T)$, $(\cdot, \cdot)_{\Gamma}$ is an inner product defined on interface Γ and $(\cdot, \cdot)_{\partial\Gamma}$ is an inner product defined on the boundary of the interface $\partial\Gamma$. Due to the kinematic boundary condition on $\partial\Gamma$ at the adhesion of interface Γ to the

capillary wall, the test function $\mathbf{v} = 0$, and due to the lack of area at the tip of the drop on the other side of $\partial\Gamma$, $(\mathbf{b}, \boldsymbol{\zeta} \cdot \mathbf{v})_{\partial\Gamma} = 0$.

The solution of the instationary term of the momentum balance for the first time step is found using a backwards Euler integration scheme, which is of first order,

$$\frac{d\mathbf{u}}{dt} = \frac{\mathbf{u}^{n+1} - \mathbf{u}^n}{\Delta t}, \tag{25}$$

using the solutions of the velocity \mathbf{u} at time t^{n+1} and t^n , respectively. The solution for all subsequent time steps will be of second order, using the second order backwards differencing method (BDF2)

$$\frac{d\mathbf{u}}{dt} = \frac{\frac{3}{2}\mathbf{u}^{n+1} - 2\mathbf{u}^n + \frac{1}{2}\mathbf{u}^{n-1}}{\Delta t}. \tag{26}$$

Herein, the solutions of the velocity \mathbf{u} at time t^{n+1} , t^n , and t^{n-1} are used. The convection term is solved iteratively. For the first iteration step, the Picard fix point iteration is used, and Newton’s method is used for the following iteration steps.

Semi-implicit time integration of the surface tension

Assuming an equilibrium between the viscous and interfacial forces, a characteristic capillary time scale can be defined as $t_{\text{capillary}} = \eta R / \gamma$. Herein, η is the bulk viscosity, R is a characteristic length scale, and γ is the interfacial tension. On element level, the capillary time scale of the problem is $t_{\text{capillary}} = \eta R / \gamma n_{\text{elem}} = \mathcal{O}(10^{-7} \text{ s})$, where $R = R_0$ and n_{elem} is the number of elements on the interface. The explicit numerical scheme is stable for time steps smaller than the capillary time scale. In order to be able to use larger time steps, the problem is written to a semi-implicit time integration scheme, as presented by Hysing (2006). Taking the contribution of the constant interfacial stress from Eq. (10) and using definitions from differential geometry, this equation can be rewritten to

$$\nabla_s \cdot \boldsymbol{\zeta} = \gamma \nabla_s^2 \mathbf{x}_{\Gamma}, \tag{27}$$

where \mathbf{x}_{Γ} is the interface position. By writing the new interface position as a function of the old position, proposed in the work of Bänsch (2001), the time discretization can be made semi-implicit

$$\mathbf{x}_{\Gamma}^{n+1} = \mathbf{x}_{\Gamma}^n + \Delta t \mathbf{u}^{n+1}. \tag{28}$$

Herein, Δt is the time step and \mathbf{u}^{n+1} is the velocity field at the new time. The interfacial stress tensor for the contribution of the surface tension becomes

$$\nabla_s \cdot \boldsymbol{\zeta} = \nabla_s \cdot (\gamma \mathbf{I}_s) + \gamma \Delta t \nabla_s^2 \mathbf{u}. \tag{29}$$

Thus, the second term of the right hand side of Eq. (29) is added to the left hand side of the system.

Movement of the mesh

Interface mesh

The movement of the interface is Lagrange based

$$\frac{dx_\Gamma}{dt} = \mathbf{u}, \tag{30}$$

where dx_Γ/dt is the velocity of the interface and \mathbf{u} is the material velocity at the interface. The discretization is done using a first order scheme

$$\frac{dx_\Gamma}{dt} = \frac{\mathbf{x}_\Gamma^{n+1} - \mathbf{x}_\Gamma^n}{\Delta t} = \mathbf{u}. \tag{31}$$

Herein, \mathbf{x}_Γ^{n+1} and \mathbf{x}_Γ^n are the coordinates of the interface at times t^{n+1} and t^n , respectively.

Bulk mesh

Since the problem has moving boundaries, the mesh is not stationary. To take the motion of the mesh into account, an Arbitrary Lagrangian Eulerian (ALE) method is applied. The material derivative of the momentum balance is changed by subtracting the grid velocity from the flow velocity in the convective term

$$\rho \frac{\delta \mathbf{u}}{\delta t} + \rho (\mathbf{u} - \mathbf{u}_{\text{grid}}) \cdot \nabla \mathbf{u} - \nabla \cdot \boldsymbol{\sigma} = \mathbf{f} \quad \text{in } \Omega \tag{32}$$

$$\nabla \cdot \mathbf{u} = 0 \quad \text{in } \Omega, \tag{33}$$

where $\delta(\cdot)/\delta t$ is the grid derivative and \mathbf{u}_{grid} is the grid velocity.

The grid velocity \mathbf{u}_{grid} for time t^{n+1} is calculated using a time discretization based on an Euler backwards differencing scheme for the first time step

$$\mathbf{u}_{\text{grid}}^{n+1} = \frac{\mathbf{x}^{n+1} - \mathbf{x}^n}{\Delta t} \tag{34}$$

and based on a BDF2 scheme for all subsequent time steps

$$\mathbf{u}_{\text{grid}}^{n+1} = \frac{\frac{3}{2}\mathbf{x}^{n+1} - 2\mathbf{x}^n + \frac{1}{2}\mathbf{x}^{n-1}}{\Delta t}. \tag{35}$$

Herein, \mathbf{x}^{n+1} , \mathbf{x}^n , and \mathbf{x}^{n-1} are the mesh coordinates on time t^{n+1} , t^n , and t^{n-1} , respectively.

The displacement of the mesh coordinates $\Delta \mathbf{x}$ is necessary to find the new mesh coordinates $\mathbf{x}^{n+1} = \mathbf{x}^n + \Delta \mathbf{x}$ and is calculated by solving a Laplace equation on the mesh. The displacement of the interface $\Delta \mathbf{x}_\Gamma = \mathbf{x}_\Gamma^{n+1} - \mathbf{x}_\Gamma^n$ is used as a boundary condition for interface Γ , while the other boundary conditions are set to zero, as shown in Fig. 1. The following set of equations is solved

$$\nabla^2 (\alpha \Delta \mathbf{x}) = 0 \quad \text{in } \Omega \tag{36}$$

$$\Delta \mathbf{x} = 0 \quad \text{on } \Gamma_{\text{in}}, \Gamma_{\text{wall}}, \text{ and } \Gamma_{\text{symmetry}} \tag{37}$$

$$\Delta \mathbf{x} = \Delta \mathbf{x}_\Gamma \quad \text{on } \Gamma \tag{38}$$

for both z - and r -direction separately. Coefficient α is a constant coefficient per element with the value $\alpha = 1/A^e$, where A^e is the area of the element (Hulsen 2015).

Remeshing, refining, and projection

When the geometry is highly deformed, the mesh may become too distorted to produce accurate solutions. To quantify the quality of the mesh, the deformation of each element is monitored, using the following equations

$$f_1^e = |\log (A^e/A_0^e)| \tag{39}$$

$$f_2^e = |\log (S^e/S_0^e)|, \tag{40}$$

where A^e and A_0^e are the element areas of the current mesh and undeformed mesh and S^e and S_0^e are the element aspect ratios of the current mesh and undeformed mesh, respectively. The aspect ratio of an element is defined as

$$S^e = (L_{\text{max}}^e)^2/A^e. \tag{41}$$

Herein, L_{max}^e is the maximum length of the sides of an element. Remeshing is performed if either $f_1^e > 0.2$ or $f_2^e > 0.2$ (Hulsen 2015).

Furthermore, the elongation of the side of each element on the interface Γ and symmetry axis is monitored by

$$f_3^e = L^e/L_0^e, \tag{42}$$

where L^e and L_0^e are the length of the sides of an element at these two curves of the current mesh and undeformed mesh, respectively. An element is refined if $f_3^e > 1.4$. The refinement is performed by adding a new node on the curve, exactly in the center between the nodes in the reference element. Subsequently, the geometry of the bulk is remeshed.

The solutions \mathbf{u}^n and \mathbf{u}^{n-1} on the new mesh are necessary to solve the implicit time integration of the Navier-Stokes equation. A projection problem is solved to acquire these solutions on the new mesh. For this projection problem,

Table 1 Refined meshes used in the mesh-convergence study

	h_{coarse} [mm]	h_{fine} [mm]	Final number of nodes
M1	0.1	0.01	6039
M2	0.05	0.005	9335
M3	0.025	0.0025	30823
M4	0.015	0.0015	81609
M5	0.01	0.001	181488
M6*	0.006	0.0006	515895

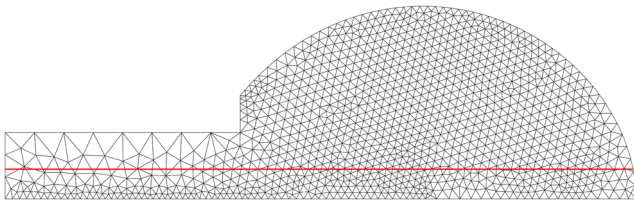


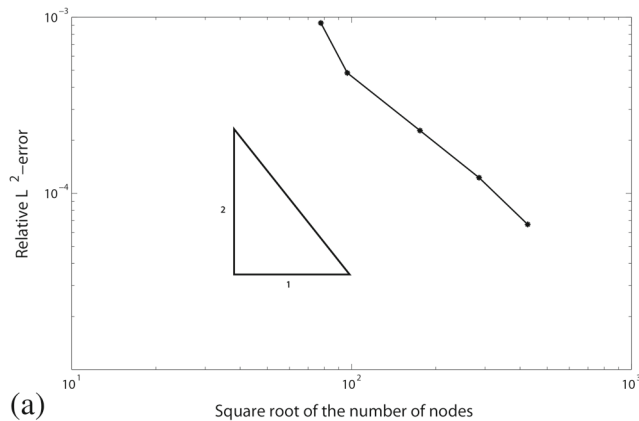
Fig. 2 Mesh M1 of the mesh-convergence study, where line Δ is given in red

field \mathbf{u} on the old mesh is defined as $\mathbf{u}^{\text{old}} = \sum_k \varphi_k^{\text{old}} \mathbf{u}_k^{\text{old}}$,

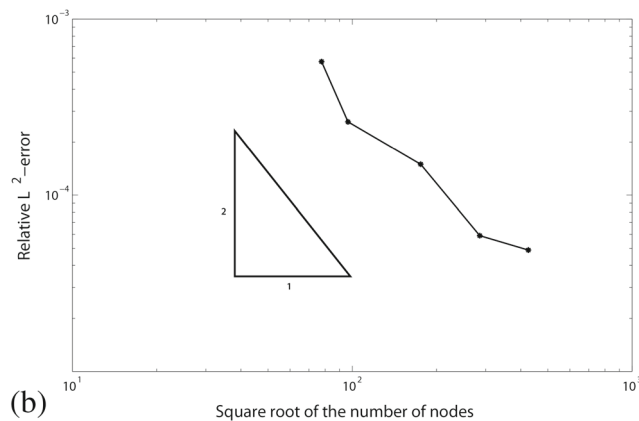
where φ_k^{old} are the shape functions on the old mesh and $\mathbf{u}_k^{\text{old}}$ are the nodal values. On the new mesh, field \mathbf{u} is defined as $\mathbf{u}^{\text{new}} = \sum_m \varphi_m^{\text{new}} \mathbf{u}_m^{\text{new}}$, where φ_m^{new} are the shape functions on the new mesh and $\mathbf{u}_m^{\text{new}}$ are the unknown nodal values on the new mesh. To find $\mathbf{u}_m^{\text{new}}$, the following problem is solved

$$\sum_m (\varphi_l^{\text{new}}, \varphi_m^{\text{new}}) \mathbf{u}_m^{\text{new}} = (\varphi_l^{\text{new}}, \mathbf{u}^{\text{old}}), \tag{43}$$

where the values of \mathbf{u}^{old} are found in the integration points defined on the new mesh.



(a)



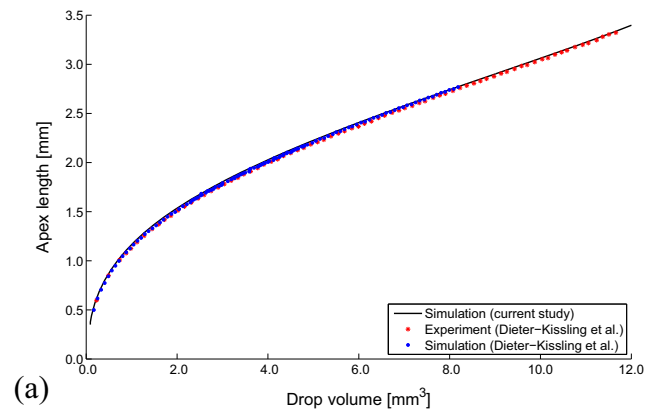
(b)

Fig. 3 Mesh-convergence of \mathbf{u} (a) and p (b)

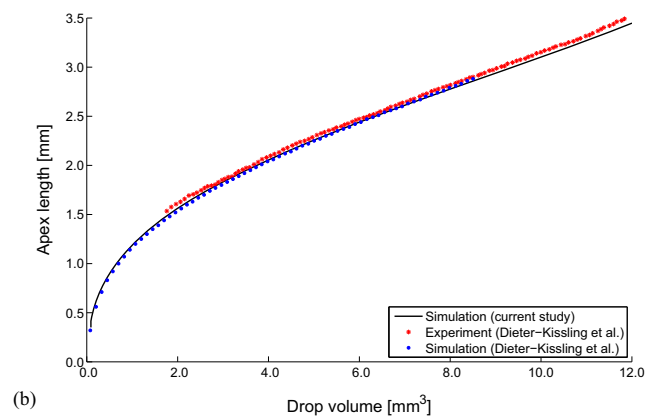
Validation

Convergence

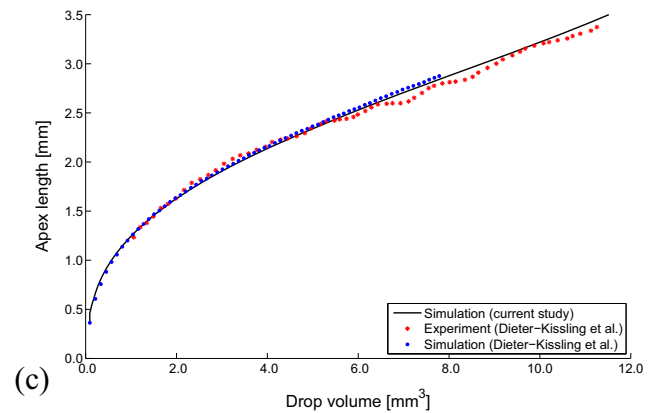
To investigate the accuracy and stability of the simulations, a mesh convergence test is performed. The velocity and pressure field are calculated until $t = 2.5 \cdot 10^{-2}$ s with a time step $\Delta t = 2.5 \cdot 10^{-4}$ s. A parabolic inflow with flow rate $Q = 42 \text{ mm}^3/\text{s}$ is prescribed. The starting mesh with mesh size $h_{\text{coarse}} = 0.1 \text{ mm}$ far away from the interface and $h_{\text{fine}} = 0.01 \text{ mm}$ on the interface boundary Γ is refined to



(a)



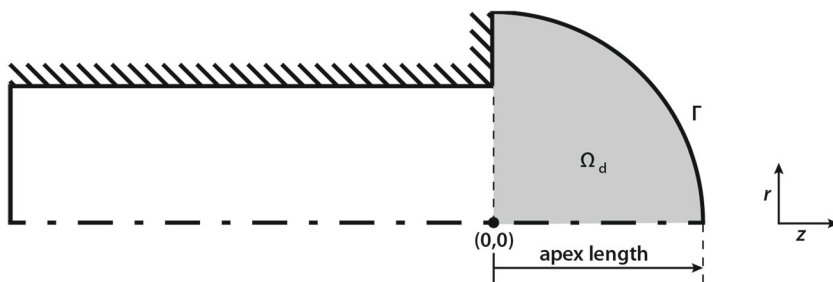
(b)



(c)

Fig. 4 Drop formation at $Q = 10 \text{ mm}^3/\text{s}$ (a), $Q = 25 \text{ mm}^3/\text{s}$ (b), and $Q = 42 \text{ mm}^3/\text{s}$ (c)

Fig. 5 Geometry $\Omega_{t=0}$ of the pendant drop, where the *gray part* Ω_d is the volume of the drop



acquire meshes with an increasing number of nodes, which can be found in Table 1. The mesh is subject to remeshing and refining during the calculations.

The relative L^2 -errors are calculated on line Λ , given by $(z, r) = (s, 0.1)$, where s is a coordinate along Λ , as shown in Fig. 2. The relative L^2 -error ϵ_u and ϵ_p for the velocities and pressures respectively are defined as

$$\epsilon_u = \frac{\left(\int_{\Lambda} \|\mathbf{u}^h - \mathbf{u}^*\|^2 ds\right)^{\frac{1}{2}}}{\left(\int_{\Lambda} \|\mathbf{u}^*\|^2 ds\right)^{\frac{1}{2}}} \tag{44}$$

$$\epsilon_p = \frac{\left(\int_{\Lambda} (p^h - p^*)^2 ds\right)^{\frac{1}{2}}}{\left(\int_{\Lambda} p^{*2} ds\right)^{\frac{1}{2}}}, \tag{45}$$

where \mathbf{u}^h and p^h are the solutions on one of the meshes given in Table 1 and \mathbf{u}^* and p^* are reference solutions computed on mesh M6*. The integrals of Eqs. (44) and (45) are computed by dividing line Λ into 10,000 intervals and using a midpoint rule on each interval. The mesh-convergence plots are shown in Fig. 3 and show that both the velocity and pressure converge with at least order two.

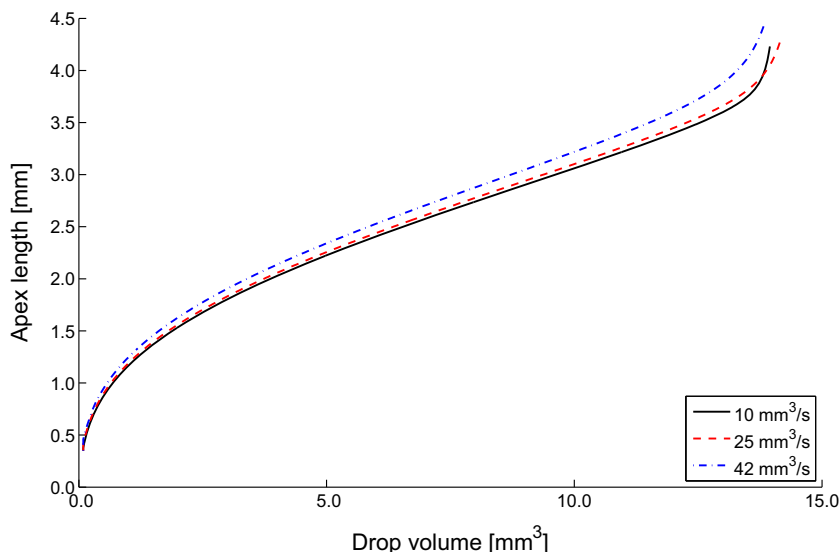
Comparison with recent results from literature

To validate the results in the case of an interface with constant surface tension, the results of this study are compared with the results of Dieter-Kissling et al. (2014). In their study, the applicability limit of the pendant drop measuring method at high inflow rates is studied. For high flow rates, the results of the Profile Analysis Tensiometry instrument appear to be invalid. Using their geometry, as shown in Fig. 1, and equal boundary conditions and parameters (as stated in the problem description), the same problems are solved to compare the results of the two computational methods. The only interface characteristic is the constant surface tension γ .

Three different flow rates are examined: $Q = 10 \text{ mm}^3/\text{s}$, $Q = 25 \text{ mm}^3/\text{s}$, and $Q = 42 \text{ mm}^3/\text{s}$. The corresponding Reynolds numbers are $Re = 28.29$, $Re = 70.73$, and $Re = 118.84$, respectively.

To compare the data of the work of Dieter-Kissling et al. (2014) with this study, the drop formation for different flow rates is investigated. The apex length is plotted versus the drop volume, as shown in Fig. 4. Both the experimental data and the data generated by the simulation of Dieter-Kissling et al. (2014) are displayed along the results of this study.

Fig. 6 Drop formation at $Q = 10 \text{ mm}^3/\text{s}$, $Q = 25 \text{ mm}^3/\text{s}$, and $Q = 42 \text{ mm}^3/\text{s}$, respectively



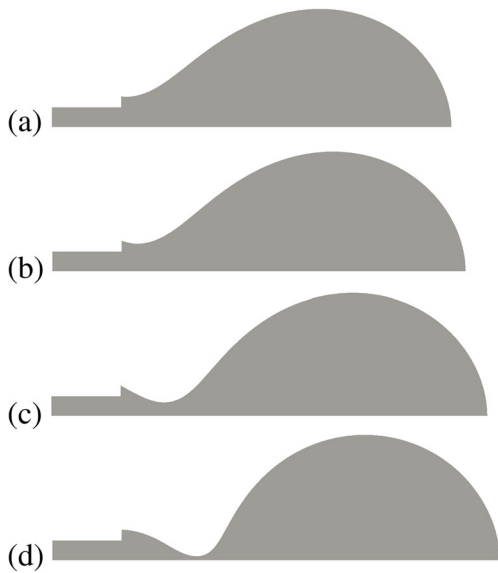


Fig. 7 Necking process for $Q = 42 \text{ mm}^3/\text{s}$ at $V = 12.85 \text{ mm}^3$ (a), $V = 13.27 \text{ mm}^3$ (b), $V = 13.69 \text{ mm}^3$ (c), and $V = 13.82 \text{ mm}^3$ (b) respectively

The volume of the drop, as depicted in Fig. 5 in gray, is calculated by

$$\begin{aligned}
 V &= \int_{\Omega_d} 1 \, dV \\
 &= \frac{1}{3} \int_{\Omega_d} \nabla \cdot \mathbf{x} \, dV \\
 &= \frac{1}{3} \oint_{\partial\Omega_d} \mathbf{n} \cdot \mathbf{x} \, dS \\
 &= \frac{1}{3} \int_{\Gamma} 2\pi r (\mathbf{n} \cdot \mathbf{x}) \, ds.
 \end{aligned} \tag{46}$$

The apex length is the z -coordinate of the apex of the drop measured from the origin. As shown in Fig. 4, the

Fig. 8 Necking radius in time for $Q = 10 \text{ mm}^3/\text{s}$, $Q = 25 \text{ mm}^3/\text{s}$, and $Q = 42 \text{ mm}^3/\text{s}$, respectively

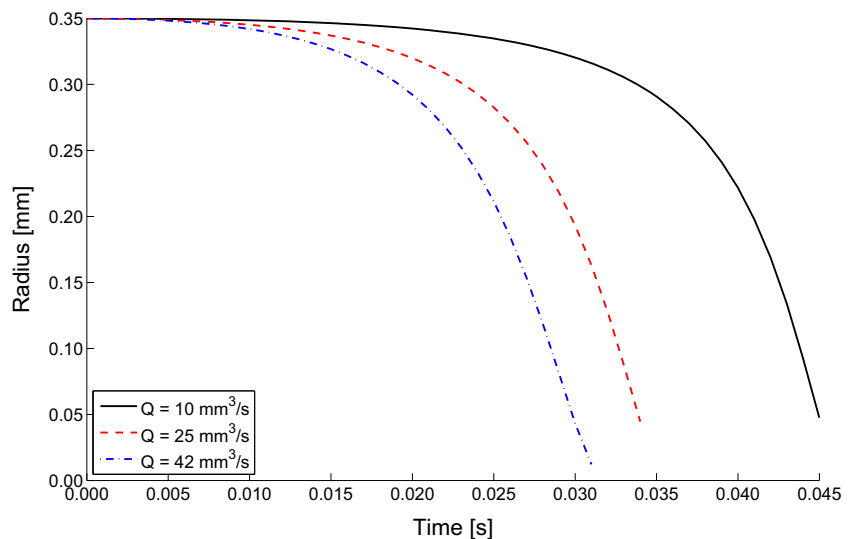


Table 2 Parameter range where the filled values denote the reference values

γ [$\mu\text{N}/\text{mm}$]	10	20	50	100
κ [$\mu\text{Ns}/\text{mm}$]	1	10	50	100
μ [$\mu\text{Ns}/\text{mm}$]	0.01	0.1	1	
K [$\mu\text{N}/\text{mm}$]	1	10	100	
G [$\mu\text{N}/\text{mm}$]	0.01	0.1	1	

drop formation of this work matches very well with both the experimental results and computational data of Dieter-Kissling et al. (2014). Our results even exceed the range of deformation of their numerical simulation.

Results

Necking

The simulations as described in the previous section are performed up until necking and the detachment of the drop. The results for the three different flow rates are shown in Fig. 6. From approximately $V = 13 \text{ mm}^3$ onward, the curves become more steep. This is where the necking occurs. In Fig. 7, the deformation of the mesh during the necking process is depicted.

For a better understanding of the necking process, the radius of the neck is plotted in time, as shown in Fig. 8, where $t = 0 \text{ s}$ is the onset of the necking process.

Detachment of the drop occurs theoretically according to the following force balance (Garandet et al. 1994)

$$\pi R^2 p + V\rho g = 2\pi R\gamma, \tag{47}$$

where p is the pressure, R is the wetted radius of the capillary, V is the volume of the drop, ρ is the density, g is

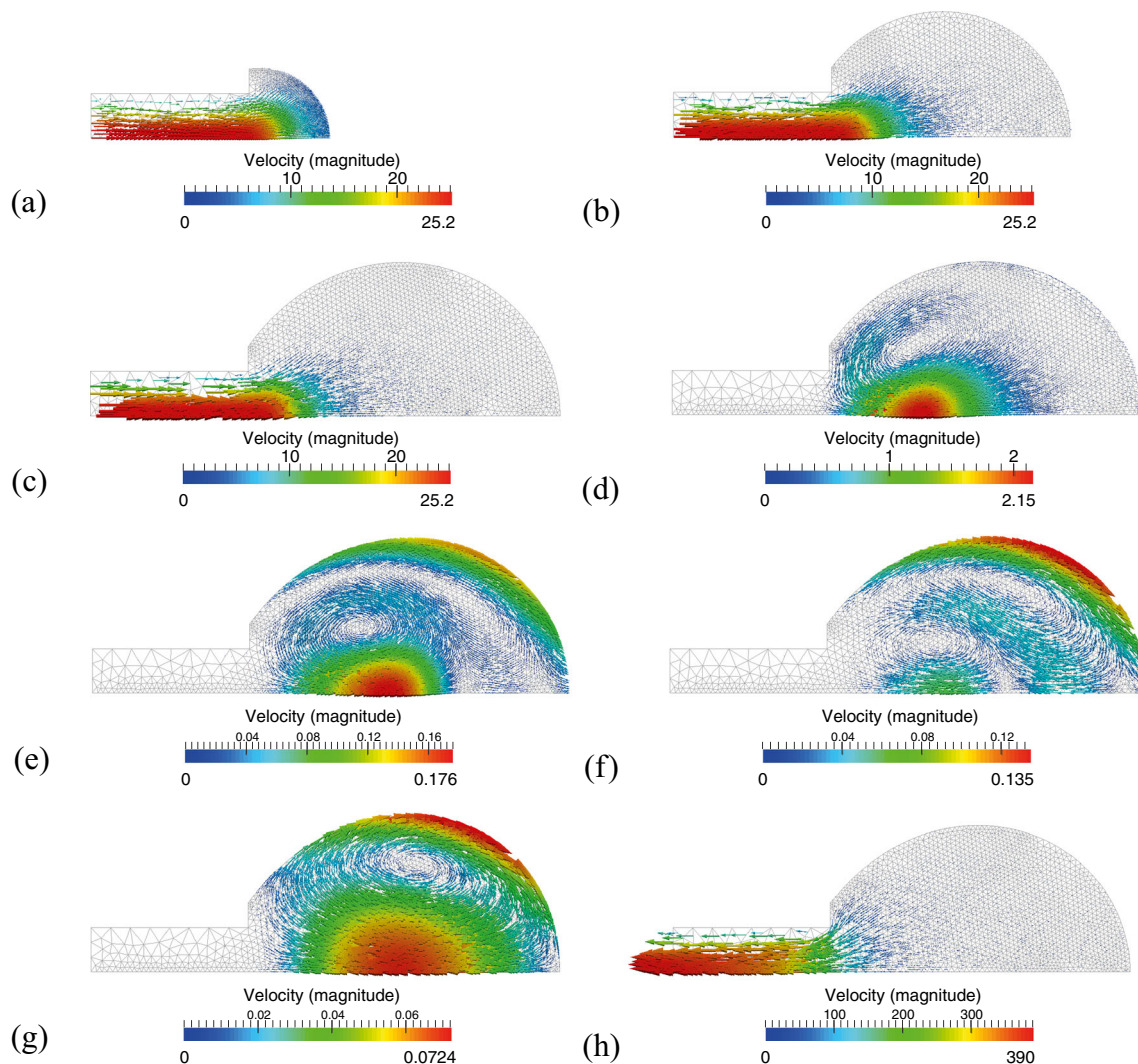


Fig. 9 Mesh and velocity for the reference state system at time $t = 0.01$ s (a), $t = 0.50$ s (b), $t = 1.00$ s (c), $t = 1.01$ s (d), $t = 1.04$ s (e), $t = 1.05$ s (f), $t = 2.00$ s (g), and $t = 2.01$ s (h), the velocity is in mm/s

the gravitational acceleration, and γ is the surface tension. The pressure at the end of the capillary is $p = 68$ Pa. From this follows that the theoretical volume for detachment of the drop is equal to $V = 13.47$ mm³, which is similar to the volume at which the necking occurs in the three simulations.

Viscoelastic interface

To investigate the influence of the five parameters of the viscoelastic constitutive model of Eq. (11), a parameter study is performed (Table 2). The ranges of the dilatational and shear viscosities and elasticities are taken from Cantat et al. (2013) and experiments performed by the group of Vermant (Verwijlen 2013). The dilatational viscosity is typically one or two orders of magnitude larger than the shear viscosity.

For an ideal elastic interface, the surface dilatational elasticity and surface shear elasticity are related to the surface Young's modulus Y according to

$$K = \frac{Y}{2(1 - \nu_s)} \quad (48)$$

$$G = \frac{Y}{2(1 + \nu_s)}, \quad (49)$$

where ν_s is the surface Poisson's ratio (Sagis 2011). Theoretically, the surface Poisson's ratio can vary between $-1 \leq \nu_s < 1$. However, for conventional materials, it holds that $0 \leq \nu_s < 1$. The ratio of the shear elasticity G and the dilatational elasticity K will therefore be $0 < G/K \leq 1$.

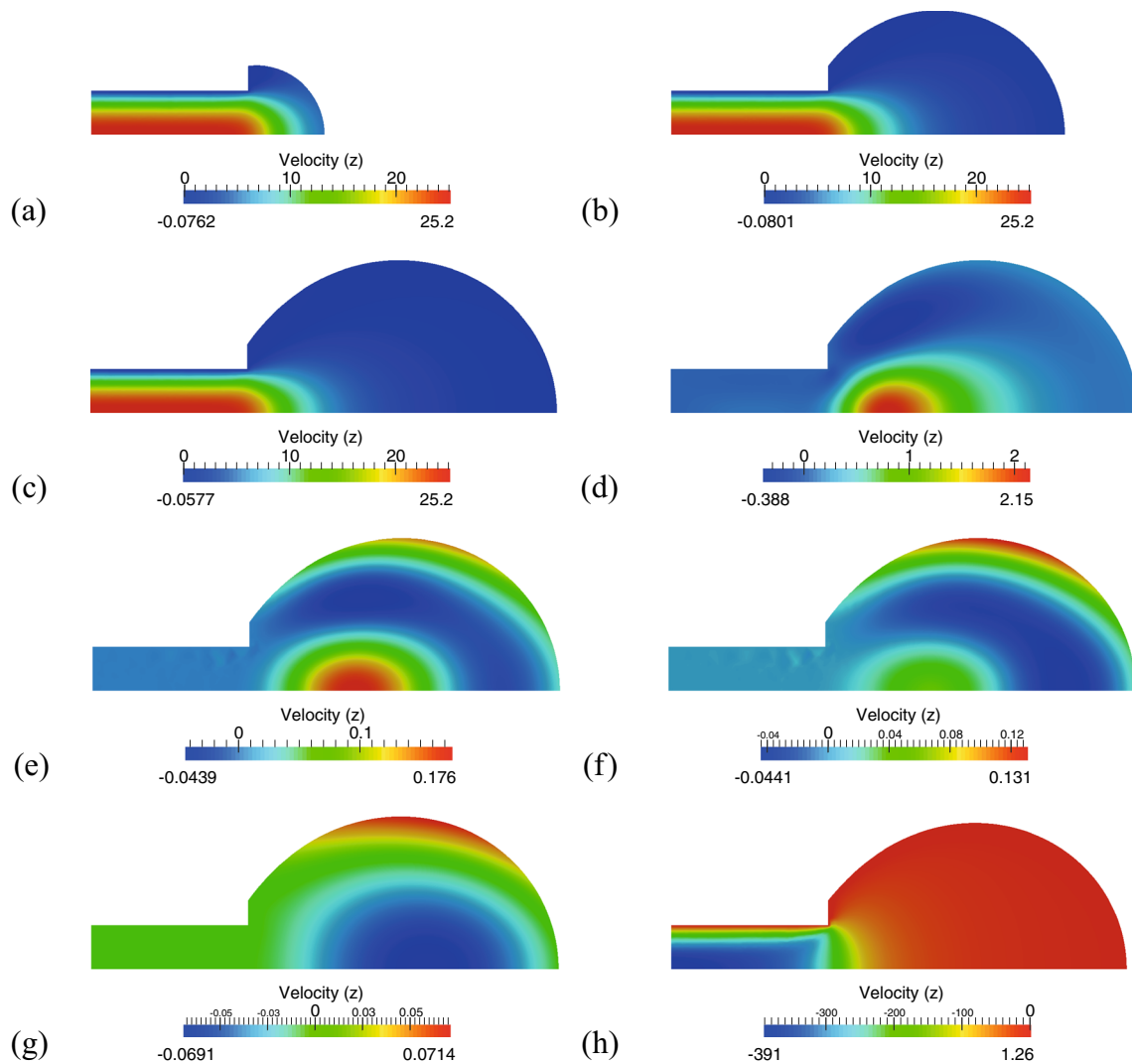


Fig. 10 Velocity in the z -direction for the reference state system at time $t = 0.01$ s, $t = 0.50$ s, $t = 1.00$ s, $t = 1.01$ s, $t = 1.04$ s, $t = 1.05$ s, $t = 2.00$ s, and $t = 2.01$ s, the velocity is in mm/s

The parameters in the gray boxes in Table 2 are chosen to be the reference state, where the ratios $\mu/\kappa = 1$ and $G/K = 1$ are upper limits. For every simulation, one parameter is changed from its reference state.

For $0 \leq t \leq 1$ s, a parabolic velocity field with flow rate $Q = 2 \text{ mm}^3/\text{s}$ is given as input. The corresponding Reynolds number is $\text{Re} = 5.66$. Subsequently, for $1 < t \leq 2$ s, a flow rate $Q = 0 \text{ mm}^3/\text{s}$ is given as input, enabling relaxation of the system. Finally, for $t > 2$ s, a pressure $p = 0 \text{ Pa}$ is set at the inlet of the capillary Γ_{in} , facilitating outflow of the fluid. For the calculations, the time step $\Delta t = 1 \cdot 10^{-3}$ s and gravitational forces are taken into account.

The mesh and the flow field of the reference state at different times are shown in Fig. 9.

In pictures (a), (b), and (c) of Fig. 9, the inflow profile is shown. In the picture (d), a vortex flowing counterclockwise can be found. This is a result of the inertial forces in the fluid. In pictures (e) and (f), a flow along the interface towards the apex is shown, resulting in a second vortex close to the apex flowing clockwise. The first vortex vanishes and the second vortex dominates the flow. During the relaxation regime, the absolute velocity decreases rapidly. In picture (h), the outflow from Γ_{in} due to the pressure difference is visible. In Figs 10, 11, and 12, the velocity in z - and r -direction, and the pressure is shown.

From simulations with the same volume using different inflow rates, the occurrence of the clockwise vortex around the apex during the relaxation regime turns out to depend on the initial flow rate; for smaller flow rates, the vortex flowing clockwise appears sooner.

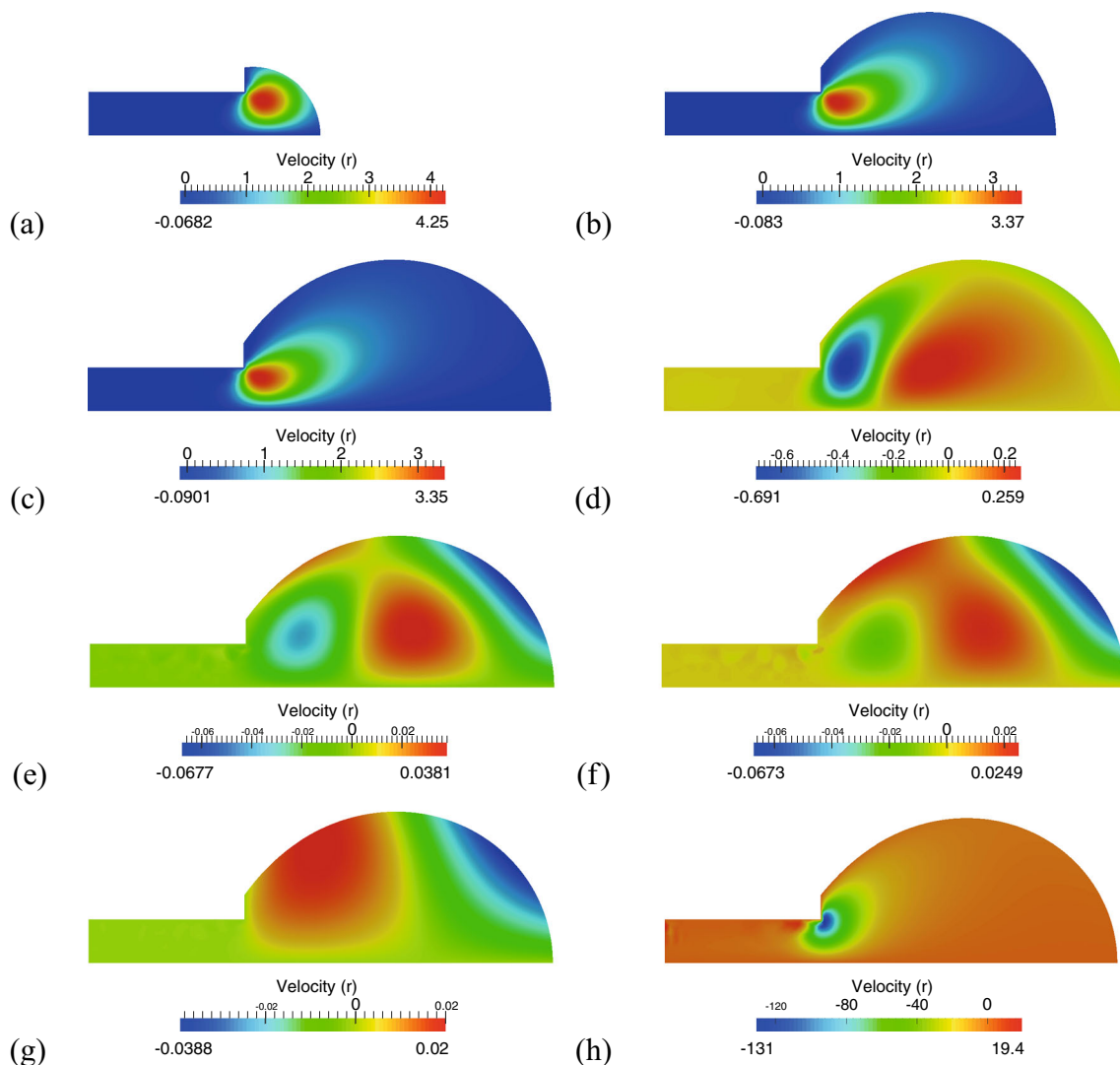


Fig. 11 Velocity in r -direction for the reference state system at time $t = 0.01$ s, $t = 0.50$ s, $t = 1.00$ s, $t = 1.01$ s, $t = 1.04$ s, $t = 1.05$ s, $t = 2.00$ s, and $t = 2.01$ s, the velocity is in mm/s

Surface tension

From the Young-Laplace equation it is known that the shape of a drop depends on the equilibrium between the gravitational forces and the surface tension. The shape of a drop should be more spherical for higher values of the surface tension, i.e., the apex length should be smaller. This behavior is found for both the inflation and relaxation of the drop as shown in Fig. 13, where the apex length in time is given for different values of the surface tension γ .

For values of the surface tension $\gamma \geq 20 \mu\text{N}/\text{mm}$, the shape of the drop remains constant during relaxation, while the drop with surface tension $\gamma = 10 \mu\text{N}/\text{mm}$ becomes more elongated and the onset of necking of the drop is visible in the relaxation time from $t = 1.80$ s. According to

Eq. (47), using a pressure $p = 14.6$ Pa at the end of the capillary, the drop will start to detach at a theoretical volume of $V = 1.67 \text{ mm}^3$. The volume of the drop during relaxation is 2.09 mm^3 .

Once the pressure at the inlet is set to $p = 0$ Pa, an outflow is generated due to the pressure difference. As shown in Fig. 13, the entire volume of the drop flows back into the capillary. For higher values of the surface tension γ , this occurs faster. The velocity of the decrease in apex length is approximately proportional to the surface tension γ .

The clockwise vortex around the apex, as described during the relaxation regime in the simulation of the reference state, occurs sooner for higher values of the surface tension γ .

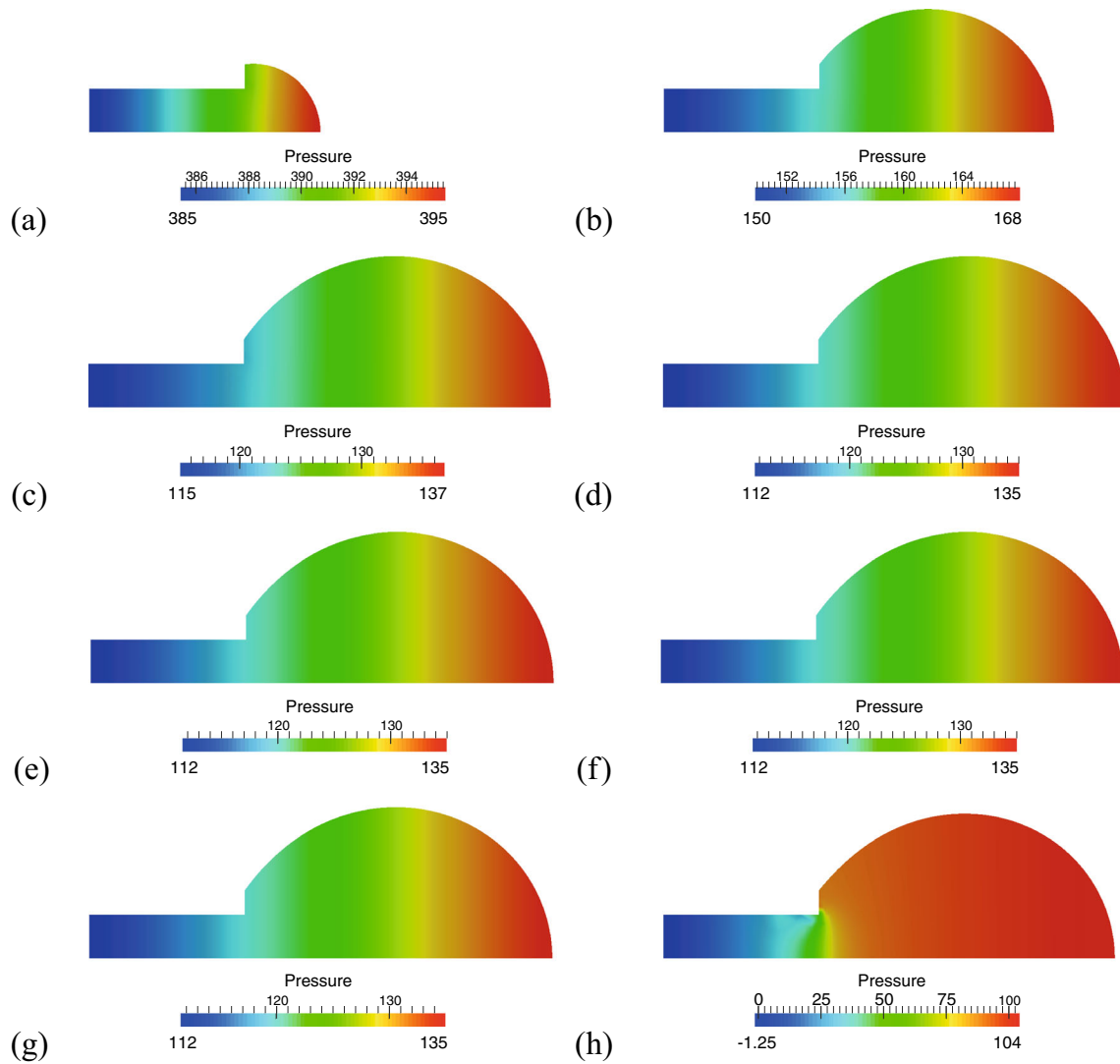


Fig. 12 Pressure for the reference state system at time $t = 0.01$ s, $t = 0.50$ s, $t = 1.00$ s, $t = 1.01$ s, $t = 1.04$ s, $t = 1.05$ s, $t = 2.00$ s, and $t = 2.01$ s, the pressure is in $\mu\text{N}/\text{mm}^2$

Fig. 13 Apex length in time for different values of the surface tension γ

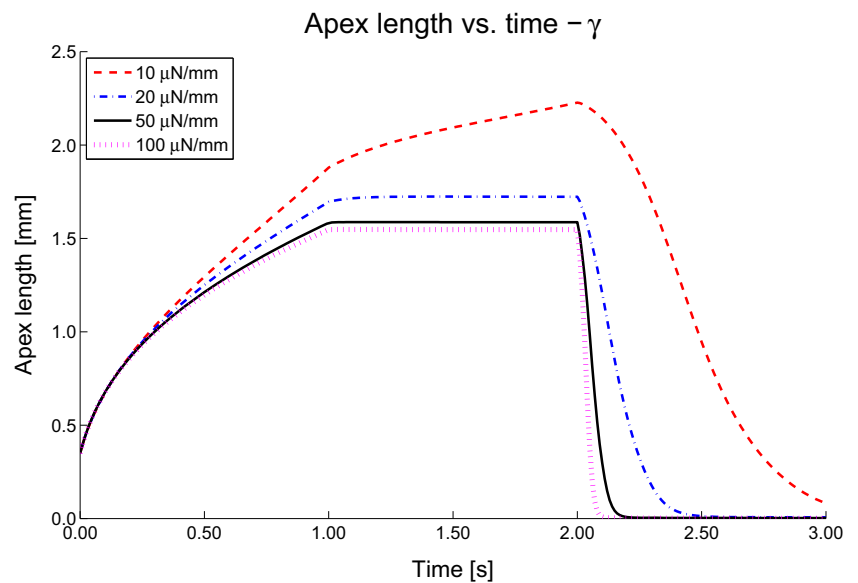


Table 3 Maximum surface strain for different values of the surface tension γ at the end of the inflow regime and the relaxation regime

γ [$\mu\text{N}/\text{mm}$]	$t = 1$ s		$t = 2$ s	
	$\max \varepsilon_t$ [-]	$\max \varepsilon_c$ [-]	$\max \varepsilon_t$ [-]	$\max \varepsilon_c$ [-]
10	7.90	1.84	12.26	1.57
20	5.66	1.77	6.66	1.51
50	4.05	1.75	4.63	1.55
100	3.46	1.76	3.94	1.56

In Table 3, the maximum values of the surface strain in both tangential and circumferential direction are given at the end of the inflow regime $t = 1$ s and at the end of the relaxation regime $t = 2$ s for different values of the surface tension γ . For smaller values of the surface tension, the maximum tangential surface strain is higher. This is due to the elongation of the drop for these small surface tension values, driven by the gravitational forces. This is shown for both the end of the inflow time and the end of the relaxation time. During the relaxation regime, the maximum tangential surface strain increases and the maximum circumferential surface strain decreases. This is due to the vortex in the bulk, moving the interface towards the apex. The influence of the surface tension on the circumferential surface strain is small.

Looking at the distribution of the surface strain, the tangential surface strain is maximum at the attachment to the capillary, while the circumferential strain is maximum between the equator and the apex of the drop. This is shown in Fig. 14.

In these calculations, the parameters for the viscoelastic behavior are nonzero. When only the surface

tension is taken into account, i.e., the parameters for the viscoelastic behavior are set to zero, holds for a surface tension $\gamma = 50 \mu\text{N}/\text{mm}$ at $t = 1$ s a maximum tangential surface strain of $\varepsilon_t = 4.55$ and a maximum circumferential surface strain of $\varepsilon_c = 2.13$. At time $t = 2$ s, the maximum tangential surface strain is $\varepsilon_t = 4.52$ and the maximum circumferential surface strain is $\varepsilon_c = 2.13$.

Surface viscosity

Viscosity is a measure of resistance to deformation. For higher viscosity, the shape of the drop should be more spherical, but should become equal for all different values of the viscosity after total relaxation. In Fig. 15, where the apex length in time is depicted for different values of the surface dilatational viscosity κ , this behavior is shown for both regimes. From Fig. 16, where the apex length in time is depicted for different values of the surface shear viscosity μ , it can be seen that the difference in behavior for the used range of values of the shear viscosity μ is negligible.

During the relaxation time, for the dilatational viscosity $\kappa \geq 50 \mu\text{Ns}/\text{mm}$, the relaxation occurs fast, as can be seen in Fig. 15.

Once the pressure at the inlet is set to $p = 0$ Pa, an outflow is generated due to the pressure difference. For the dilatational viscosity $\kappa \geq 50 \mu\text{Ns}/\text{mm}$, the shape becomes more elongated although the volume decreases. This is due to a flow in negative radial direction in the region of the drop just outside the capillary and the resistance to deformation of the interface. This radial flow initializes necking and “collapsing” of the drop, while the interface withstands the change in area. The flow field for $\kappa = 100 \mu\text{Ns}/\text{mm}$ at the start of the outflow regime is shown in Fig. 17. For higher

Fig. 14 Strain distribution for the tangential surface strain and the circumferential surface strain for surface tension $\gamma = 10 \mu\text{N}/\text{mm}$ (left) and $\gamma = 50 \mu\text{N}/\text{mm}$ (right) at time $t = 1$ s

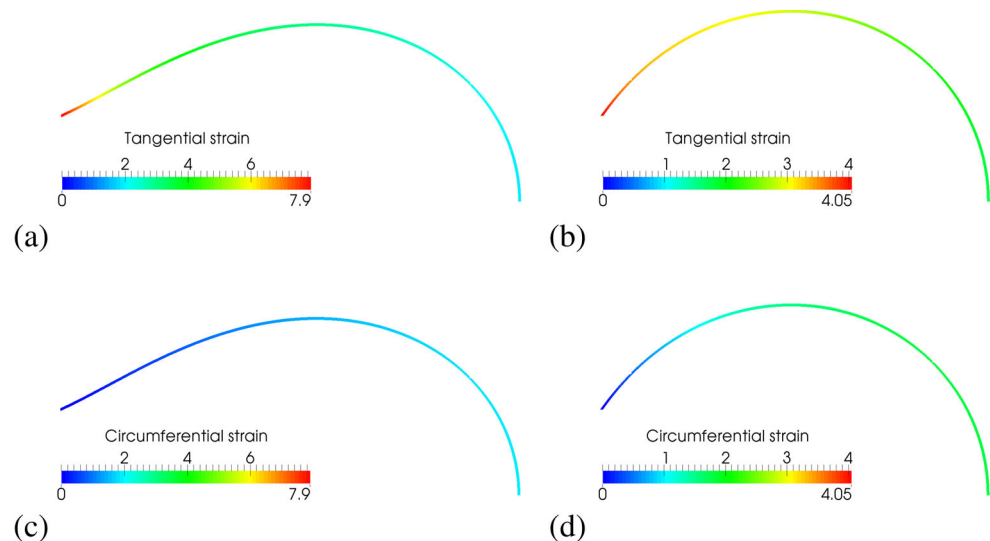
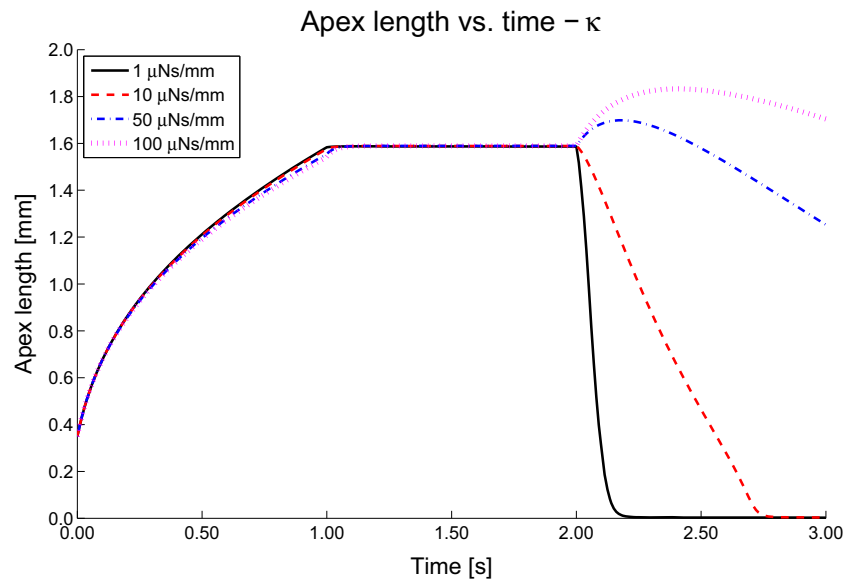


Fig. 15 Apex length in time for different values of the surface dilatational viscosity κ



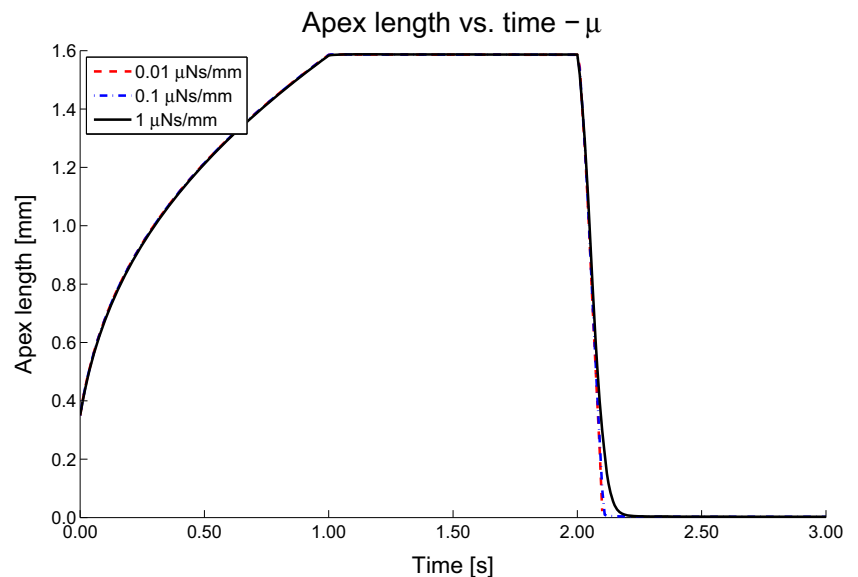
shear viscosity μ , the decrease in volume is slower than for lower shear viscosity μ .

The clockwise vortex around the apex, as described during the relaxation regime in the simulation of the reference state, occurs later for larger values of the dilatational viscosity κ , the absolute value of the velocity is lower and originates at a larger distance from the interface. The different values for the shear viscosity μ have little influence on the flow field of the drop.

The maximum values of the surface strain in both tangential and circumferential direction are given at the end of the inflow regime $t = 1$ s and at the end of the relaxation regime $t = 2$ s for different values of the dilatational viscosity κ in Table 4 and for different values of the shear viscosity

μ in Table 5. The influence of the dilatational viscosity on the tangential surface strain is small. For larger values of the dilatational viscosity, the maximum circumferential surface strain is larger. This is shown for both the end of the inflow time and the end of the relaxation time. For higher values of the shear viscosity, the tangential surface strain is smaller and the circumferential surface strain is larger. This is shown for both the end of the inflow time and the end of the relaxation time as well. During the relaxation regime, the vortex in the bulk moves the interface toward the apex, resulting in an increase of the maximum tangential surface strain and a decrease of the maximum circumferential surface strain. This is observed for both the different values of the dilatational viscosity κ and the different values of the shear viscosity μ .

Fig. 16 Apex length in time for different values of the surface shear viscosity μ



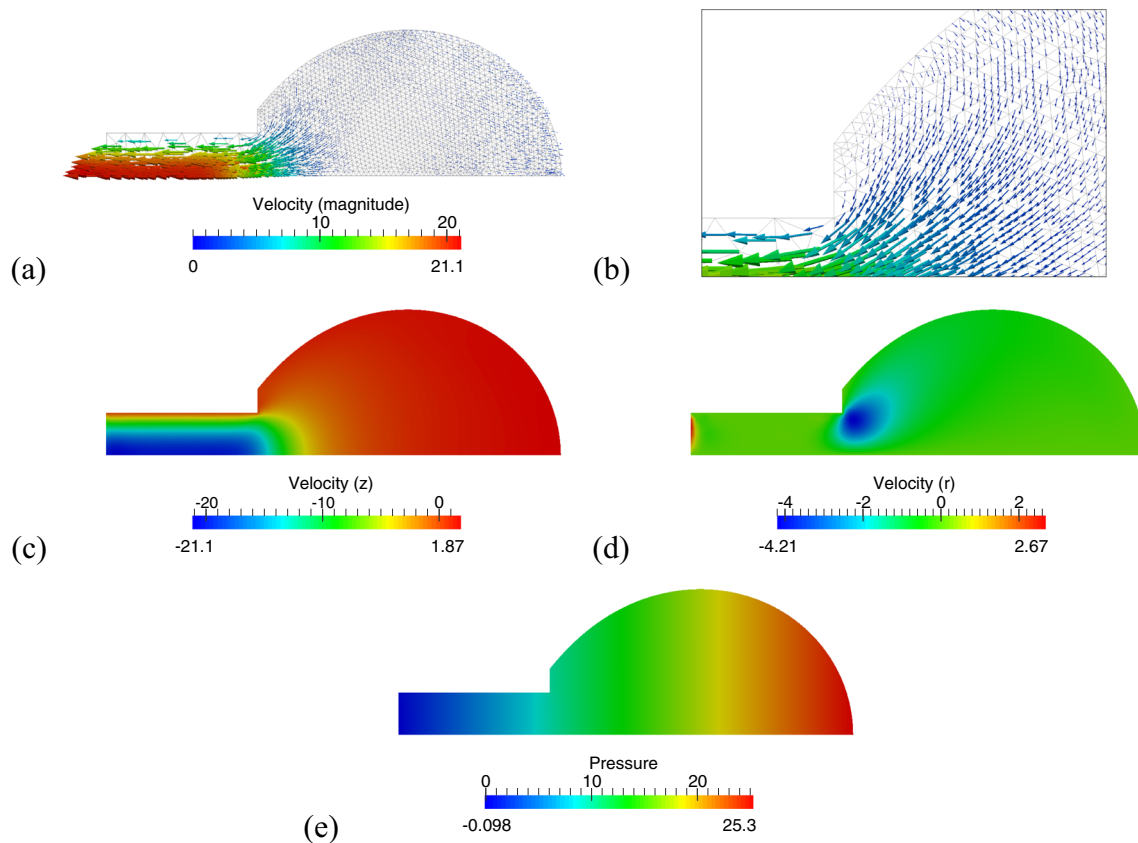


Fig. 17 Flow field for $\kappa = 100 \mu\text{Ns}/\text{mm}$ at time $t = 2.01 \text{ s}$ (a), a close up of the region at the end of the capillary (b), the velocity in z - (c) and r -direction (d), and the pressure (e)

Surface elasticity

Elasticity is the tendency of materials to return to their original shape, i.e., their state of zero stress. In this study, this state is given by the geometry $\Omega_{t=0}$ of Fig. 1. For higher elasticity, the shape of the drop should be more spherical during inflation. During the relaxation time, the shape should not change anymore. This behavior is shown in Fig. 18, where the apex length in time for different values of

the surface dilatational elasticity K is displayed. In Fig. 19, the apex length in time is shown for different values of the surface shear elasticity G . As depicted, the difference in behavior for the used range of values of the shear elasticity G is negligible.

Since a larger pressure is needed for higher values of the dilatational elasticity K , the outflow velocity is higher once the pressure is set to $p = 0 \text{ Pa}$ at the inlet. This results in a faster decrease in volume and apex length. For values of the dilatational elasticity $K \leq 10 \mu\text{N}/\text{mm}$, the surface tension seems to dominate the outflow behavior, since the volume

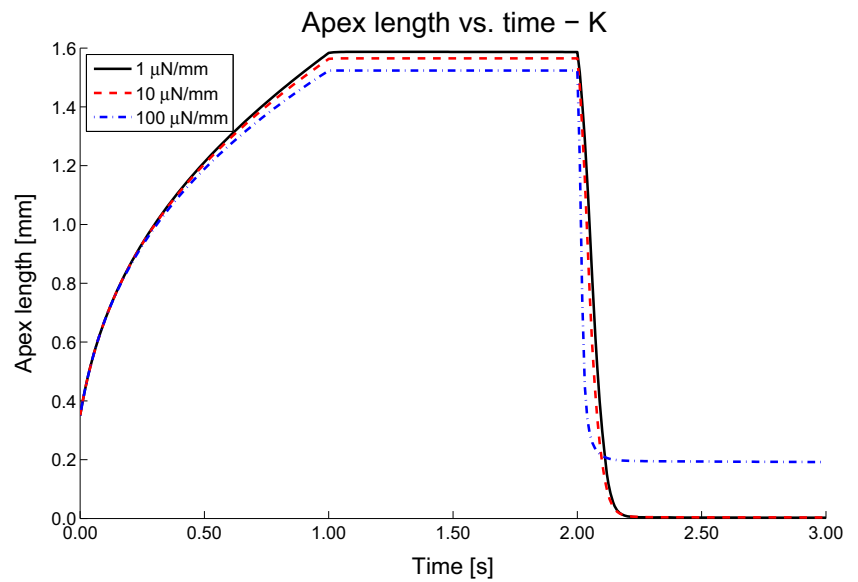
Table 4 Maximum surface strain for different values of the dilatational viscosity κ at the end of the inflow regime and the relaxation regime

κ [$\mu\text{Ns}/\text{mm}$]	$t = 1 \text{ s}$		$t = 2 \text{ s}$	
	$\max \varepsilon_t$ [–]	$\max \varepsilon_c$ [–]	$\max \varepsilon_t$ [–]	$\max \varepsilon_c$ [–]
1	4.05	1.75	4.63	1.55
10	4.34	2.05	4.60	1.94
50	4.11	2.11	4.72	2.09
100	3.89	2.12	4.74	2.11

Table 5 Maximum surface strain for different values of the shear viscosity μ at the end of the inflow regime and the relaxation regime

μ [$\mu\text{Ns}/\text{mm}$]	$t = 1 \text{ s}$		$t = 2 \text{ s}$	
	$\max \varepsilon_t$ [–]	$\max \varepsilon_c$ [–]	$\max \varepsilon_t$ [–]	$\max \varepsilon_c$ [–]
0.01	5.08	1.54	5.18	1.45
0.1	4.95	1.56	5.13	1.46
1	4.05	1.75	4.63	1.55

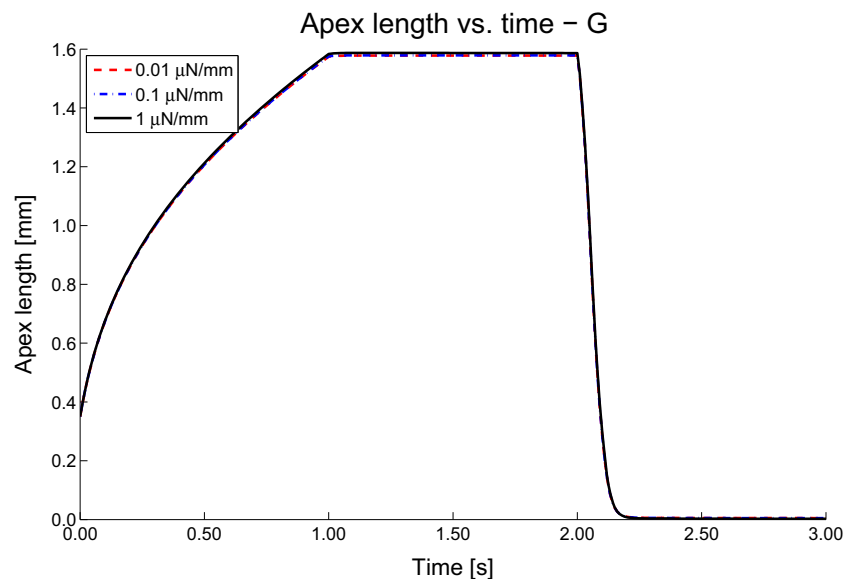
Fig. 18 Apex length in time for different values of the surface dilatational elasticity K



of the drop decreases to zero. For dilatational elasticity $K = 100 \mu\text{N}/\text{mm}$, an equilibrium between the elasticity and the surface tension is reached before the volume of the drop is decreased to zero. As shown in Fig. 19, the difference in outflow behavior for the used range of values of the shear elasticity G is negligible.

The clockwise vortex around the apex, as described during the relaxation regime in the simulation of the reference state, occurs later for larger values of the dilatational elasticity K and the absolute value of the velocity is lower. For $K = 100 \mu\text{N}/\text{mm}$, the velocity is already zero before the vortex can occur. For larger values of the shear elasticity G , the clockwise vortex around the apex occurs sooner and the absolute value of the velocity is higher.

Fig. 19 Apex length in time for different values of the surface shear elasticity G



In Table 6, the maximum values of the surface strain in both tangential and circumferential directions are given at the end of the inflow regime $t = 1 \text{ s}$ and at the end of the relaxation regime $t = 2 \text{ s}$ for different values of the dilatational elasticity K and for different values of the shear elasticity G this is shown in Table 7. The influence of both the dilatational and shear elasticity on the tangential surface strain is small. For larger values of the dilatational elasticity, the maximum circumferential surface strain is larger, while for larger values of the shear elasticity, the maximum circumferential surface strain is smaller. During the relaxation regime, the vortex in the bulk moves the interface toward the apex, resulting in an increase of the maximum tangential surface strain and a decrease of the maximum circumferential surface strain. This is observed for both the different

Table 6 Maximum surface strain for different values of the dilatational elasticity K at the end of the inflow regime and the relaxation regime

K [$\mu\text{N}/\text{mm}$]	$t = 1$ s		$t = 2$ s	
	ε_t [–]	ε_c [–]	ε_t [–]	ε_c [–]
1	4.05	1.75	4.63	1.55
10	4.27	2.00	4.38	1.99
100	3.58	2.12	3.59	2.12

values of the dilatational elasticity $K \leq 10 \mu\text{N}/\text{mm}$ and the different values of the shear elasticity G .

Elevated values of the interface parameters

The same flow regime as described in the previous section is carried out for elevated values of the surface dilatational and shear viscosity and elasticity. The surface tension is kept at $\gamma = 50 \mu\text{N}/\text{mm}$. For simulations with elevated surface viscosities, the dilatational viscosity is set to $\kappa = 100 \mu\text{Ns}/\text{mm}$, and the shear viscosity is varied between $1 \leq \mu \leq 100 \mu\text{Ns}/\text{mm}$, while the surface elasticities are kept at $K = G = 1 \mu\text{N}/\text{mm}$. Similarly, for simulations with elevated surface elasticities, the dilatational elasticity is set to $K = 100 \mu\text{N}/\text{mm}$, and the shear elasticity is varied between $1 \leq G \leq 100 \mu\text{N}/\text{mm}$, while the surface viscosities are kept at $\kappa = \mu = 1 \mu\text{Ns}/\text{mm}$. For flow situations where the drop undergoes very large deformation, the results obtained are limited by the quasi-linear constitutive equation, and future work is focussed on developing more realistic interfacial constitutive relations.

Surface viscosity

As stated in “[Surface viscosity](#)”, for higher surface viscosity, the shape of the drop should be more spherical during the inflow regime, but should become equal for all different values of the viscosity after total relaxation. In Fig. 20,

Table 7 Maximum surface strain for different values of the shear elasticity G at the end of the inflow regime and the relaxation regime

G [$\mu\text{N}/\text{mm}$]	$t = 1$ s		$t = 2$ s	
	ε_t [–]	ε_c [–]	ε_t [–]	ε_c [–]
0.01	3.73	2.33	4.21	2.23
0.1	3.76	2.27	4.23	2.14
1	4.05	1.75	4.63	1.55

where the apex length in time is depicted for different values of the surface shear viscosity μ , this behavior is shown for the inflow regime. For values of $\mu \geq 10 \mu\text{Ns}/\text{mm}$, it can be seen that a relaxation time of 1 s is not sufficient for the flow to fully relax. During the outflow regime, only for $\mu = 1 \mu\text{Ns}/\text{mm}$, the figure shows that the shape of the drop becomes more elongated although the volume decreases. For more elevated values, the surface shear viscosity might prevent the “collapsing” of the drop.

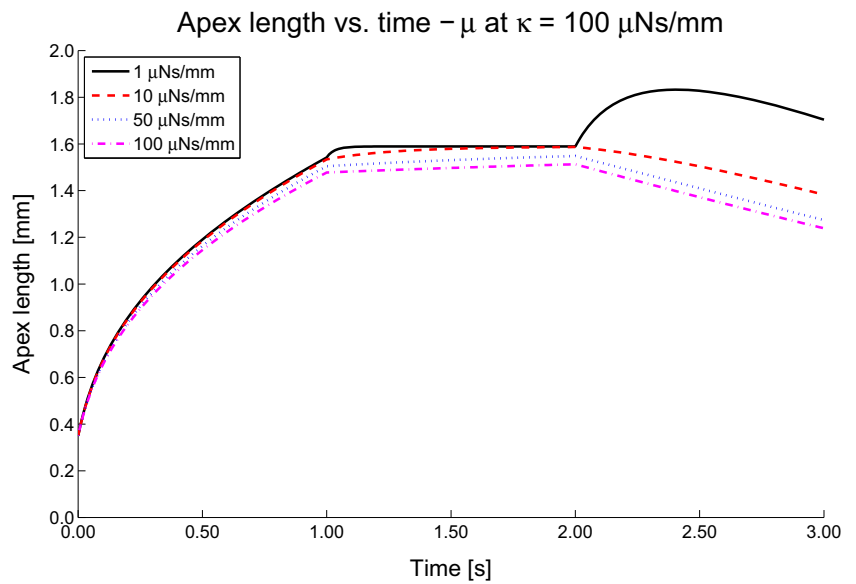
Surface elasticity

As shown in Fig. 21, where the apex length in time is depicted for different values of the surface shear elasticity, the drop becomes more elongated during the inflow regime for increasing values of the elasticity. This is contradictory to the expectation that the shape of the drop should be more spherical during inflation, as stated in “[Surface elasticity](#)”. For $G = 100 \mu\text{N}/\text{mm}$, a sharp slope transition can be observed. In this case, the resistance of interface deformation in r -direction is more profound than in z -direction, resulting initially in a flow in z -direction only, before flowing in r -direction. During the relaxation time, the shape of the drop does not change anymore, as expected. For shear elasticity $G = 1 \mu\text{N}/\text{mm}$, the equilibrium between the elasticity and the surface tension is reached before the volume of the drop is decreased to zero, as is seen in “[Surface elasticity](#)” as well. For values of $G \geq 10 \mu\text{N}/\text{mm}$, the shape of the drop becomes more elongated during the outflow regime, and the simulations end before the prescribed time is over. This is due to the numerical boundary condition that states that the interface is fixed to the outer edge of the capillary; the fluid layer on the wetted tip of the capillary becomes too thin to be properly calculated.

Oscillatory measurements

To connect the presented model to experimental methods for testing the interface characteristics, a small amplitude oscillatory measurement is simulated with different interfacial properties. For $0 \leq t \leq 0.5$ s, a parabolic velocity field with flow rate $Q = 2 \text{ mm}^3/\text{s}$ is given as input at Γ_{in} . After that, a flow rate $Q = 0 \text{ mm}^3/\text{s}$ is given as input for $0.5 < t \leq 1$ s, enabling relaxation of the system. For the next 12π seconds, a parabolic velocity field with oscillating flow rate $Q = 0.1 \cos(0.5t) \text{ mm}^3/\text{s}$ is prescribed. This simulation is performed for the case of only a surface tension of $\gamma = 50 \mu\text{N}/\text{mm}$, the reference state as described in “[Viscoelastic interface](#)”, the reference state with $\kappa = 100 \mu\text{Ns}/\text{mm}$ as the only changed parameter, and the

Fig. 20 Apex length in time for different values of the surface shear viscosity μ at a surface dilatational viscosity $\kappa = 100 \mu\text{Ns}/\text{mm}$

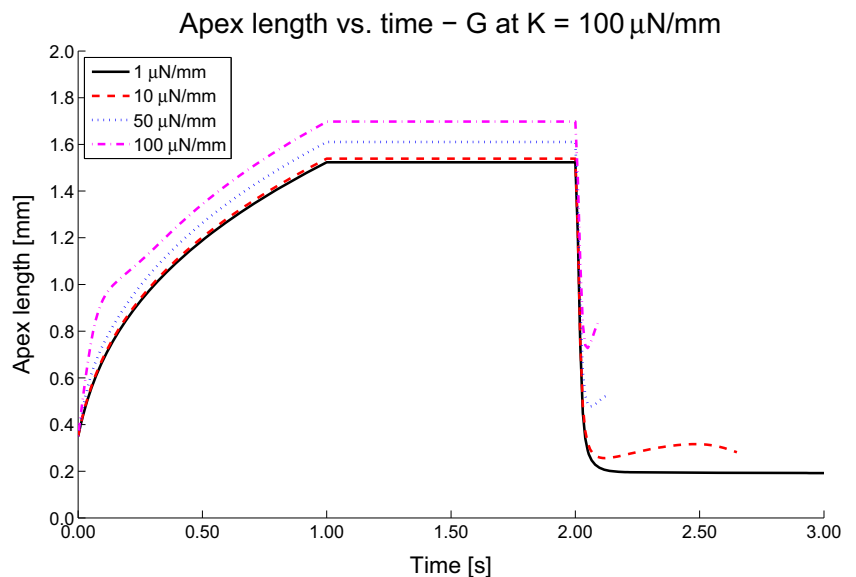


reference state with $K = 100 \mu\text{N}/\text{mm}$ as the only changed parameter. The results are shown in Fig. 22, where V is the volume of the drop, L_{apex} is the apex length, p is the pressure at the inlet Γ_{in} , and R is the radius of curvature at the apex. The subscript eq indicates the value of the variables at $t = 1 \text{ s}$.

Figure 22 shows that the responses of the apex length, the pressure, and the radius of curvature to an oscillating volume are nearly sinusoidal. For the cases (a), (b), and (d), the pressure is out of phase compared to

the radius by approximately π radians. This is in accordance with the findings of Kotula and Anna (2015): for a purely elastic interface limit of $\kappa = 0 \mu\text{Ns}/\text{mm}$, the phase shift goes to π radians. Furthermore, from Kotula and Anna (2015) follows that a phase shift of $\pi/2$ is the limiting case when the dilatational viscosity is much greater than the surface tension. In case (c), where the dilatational viscosity $\kappa = 100 \mu\text{Ns}/\text{mm}$ is higher than the surface tension $\gamma = 50 \mu\text{N}/\text{mm}$, the phase shift tends towards $\pi/2$ radians.

Fig. 21 Apex length in time for different values of the surface shear elasticity G at a surface dilatational elasticity $K = 100 \mu\text{N}/\text{mm}$



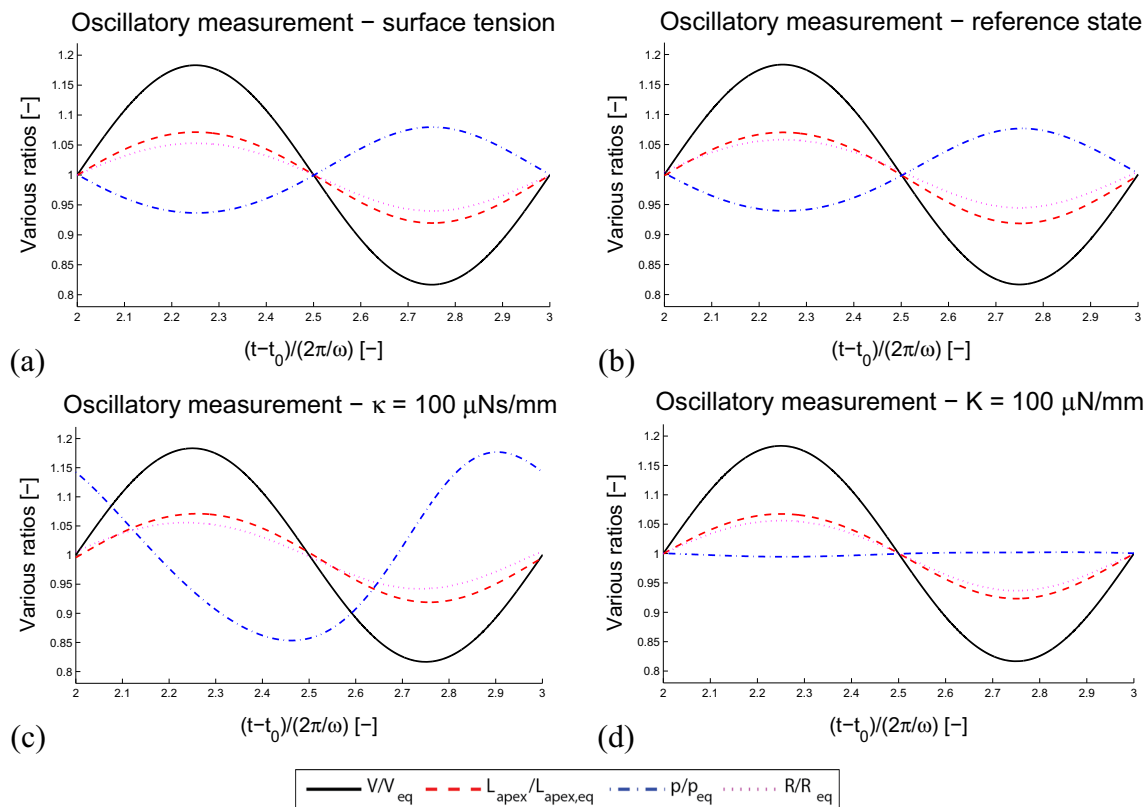


Fig. 22 Simulated responses of the normalized volume V/V_{eq} , the apex length $L_{apex}/L_{apex,eq}$, pressure p/p_{eq} , and radius of curvature R/R_{eq} , due to an oscillating flow rate Q with amplitude $a = 0.1 \text{ mm}^3$ and angular frequency $\omega = 0.5 \text{ rad/s}$, for only a surface tension of

$\gamma = 50 \mu\text{N/mm}$ (a), the reference state (b), the reference state with $\kappa = 100 \mu\text{Ns/mm}$ (c), and the reference state with $K = 100 \mu\text{N/mm}$ (d). The results of the third oscillation cycles are plotted in the time domain shifted by a time $t_0 = 1 \text{ s}$

Conclusions

In this study, a two-dimensional axisymmetric model is developed to simulate pendant drop experiments using a finite element method. In this model, the dynamics of the interface are described by a Lagrange-based interface tracking model. Furthermore, the quality of the mesh is monitored, and mesh refinement is performed if necessary. A semi-implicit time integration scheme is used to calculate the surface tension to cope with the small capillary time scale of the problem. The model is verified with the results as presented in a publication by Dieter-Kissling et al. (2014) for a Newtonian fluid in a Navier-Stokes flow, with gravitational forces and constant surface tension. A quasi-linear two-dimensional Kelvin-Voigt viscoelastic constitutive model is implemented at the interface, following Verwijlen et al. (2014). The model is made quasi-linear by using a combination of two finite strain tensors; the Hencky strain tensor is used for the dilatational contribution and the Green-Lagrange strain tensor is used to describe the shear contribution. A computational tool is designed to calculate the tangential and circumferential surface strain to quantify the deformation of the interface.

A parameter study is performed to investigate the influence of the five parameters of the quasi-linear two-dimensional Kelvin-Voigt model: the surface tension γ , the surface dilatational viscosity κ , the surface shear viscosity μ , the surface dilatational elasticity K , and surface shear elasticity G . During inflation, the apex length of the drop is significantly smaller for higher values of the surface tension and the dilatational elasticity, and is slightly smaller for higher values of the surface dilatational viscosity. Unless the force balance at the outlet of the capillary initiates the onset of detachment, the shape of the drop stayed at an equilibrium state during relaxation for different values of the surface tension and dilatational elasticity. For all different values of the dilatational viscosity, the shape of the drop became equal after total relaxation. For higher values of the surface tension, the entire volume of the drop flowed back into the capillary faster. The decrease of the apex length during the outflow regime was slower for higher values of the dilatational viscosity. For values $\kappa \geq 50 \mu\text{Ns/mm}$, the apex length increased at first due to a flow in negative radial direction in the region of the drop just outside the capillary and the resistance to deformation of the interface. The surface tension seemed to dominate the outflow behavior for

values of the dilatational elasticity $K \leq 10 \mu\text{N}/\text{mm}$. For higher values of the dilatational elasticity, an equilibrium between the elasticity and the surface tension is reached during the outflow regime. The influence of both the shear viscosity and the shear elasticity on the apex length is negligible for the used parameter range.

For elevated values of the surface viscosities and elasticities, the higher values of the surface shear viscosity delay the relaxation and prevent the drop to “collapse”, while increasing surface shear elasticities give rise to a more elongated shape during both the inflow and outflow regime.

A small amplitude oscillatory measurement is simulated. The phase shift between the response of the radius of curvature and the pressure for more elastic interfaces is approximately π radians, while for dominant dilatational viscosity the phase shift tends towards $\pi/2$ radians.

The simulations should be compared with experimental results. A relevant example of surface active agent with viscoelastic behavior is the protein hydrophobin (HFBII) (Alexandrov et al. 2012; Danov et al. 2015; Knoche et al. 2013); it forms a film of high mechanical strength when adsorbed to the interface. Furthermore, the geometry from the numerical computations could be used as input for the experimental software, to compare the input parameters of the model with the solutions from the experimental setup.

Acknowledgments The authors sincerely acknowledge M.R. Hashemi for the initial discussions on the numerical aspects of this work. In addition, we thank D. Bothe and coworkers for providing the raw data of Fig. 4. Finally, the authors thank the reviewers for their suggestion to simulate oscillatory flow and their constructive comments which resulted in an improved version of our manuscript.

Open Access This article is distributed under the terms of the Creative Commons Attribution 4.0 International License (<http://creativecommons.org/licenses/by/4.0/>), which permits unrestricted use, distribution, and reproduction in any medium, provided you give appropriate credit to the original author(s) and the source, provide a link to the Creative Commons license, and indicate if changes were made.

References

- Aland S, Lowengrub J, Voigt A (2011) A continuum model of colloid-stabilized interfaces. *Phys Fluids* 23(6):062103
- Alexandrov NA, Marinova KG, Gurkov TD, Danov KD, Kralchevsky PA, Stoyanov SD, Blijdenstein TBJ, Arnaudov LN, Pelan EG, Lips A (2012) Interfacial layers from the protein HFBII hydrophobin: dynamic surface tension, dilatational elasticity and relaxation times. *J Colloid Interface Sci* 376(1):296–306
- Bänsch E (2001) Finite element discretization of the Navier-Stokes equations with a free capillary surface. *Numer Math* 88(2):203–235
- Barthès-Biesel D, Rallison JM (1981) The time-dependent deformation of a capsule freely suspended in a linear shear flow. *J Fluid Mech* 113:251–267
- Bazhlekov IB, Anderson PD, Meijer HEH (2006) Numerical investigation of the effect of insoluble surfactants on drop deformation and breakup in simple shear flow. *J Colloid Interface Sci* 298(1):369–394
- Bos MA, Van Vliet T (2001) Interfacial rheological properties of adsorbed protein layers and surfactants: a review. *Adv Colloid Interf Sci* 91(3):437–471
- Cantat I, Cohen-Addad S, Elias F, Graner F, Höhler R, Pitois O, Rouyer F (2013) *Foams: structure and dynamics*. Oxford University Press, Oxford
- Danov KD, Stanimirova RD, Kralchevsky PA, Marinova KG, Alexandrov NA, Stoyanov SD, Blijdenstein TBJ, Pelan EG (2015) Capillary meniscus dynamometry—method for determining the surface tension of drops and bubbles with isotropic and anisotropic surface stress distributions. *J Colloid Interface Sci* 440:168–178
- Derkach SR, Krägel J, Müller R (2009) Methods of measuring rheological properties of interfacial layers (experimental methods of 2D rheology). *Colloid J* 71(1):1–17
- Dieter-Kissling K, Karbaschi M, Marschall H, Javadi A, Müller R, Bothe D (2014) On the applicability of drop profile analysis tensiometry at high flow rates using an interface tracking method. *Colloids Surf A Physicochem Eng Asp* 441:837–845
- Drelich J, Fang CH, White CL (2002) Measurement of interfacial tension in fluid–fluid systems. *Encyclopedia of Surface and Colloid Science*:3152–3166
- Eggleton CD, Tsai TM, Stebe KJ (2001) Tip streaming from a drop in the presence of surfactants. *Physical Review Letters* 87(4):048302
- Erni P, Jerri HA, Wong K, Parker A (2012) Interfacial viscoelasticity controls buckling, wrinkling and arrest in emulsion drops undergoing mass transfer. *Soft Matter* 8(26):6958–6967
- Fuller GG, Vermant J (2011) Editorial: dynamics and rheology of complex fluid–fluid interfaces. *Soft Matter* 7(17):7583–7585
- Garandet JP, Vinet B, Gros P (1994) Considerations on the pendant drop method: a new look at Tate’s law and Harkins’ correction factor. *J Colloid Interface Sci* 165(2):351–354
- Hulsen MA (2015) *TFEM, A toolkit for the finite element method: user’s guide*. Eindhoven University of Technology, Eindhoven
- Hysing S (2006) A New implicit surface tension implementation for interfacial flows. *Int J Numer Methods Fluids* 51(6):659–672
- James AJ, Lowengrub J (2004) A Surfactant-conserving volume-of-fluid method for interfacial flows with insoluble surfactant. *J Comput Phys* 201(2):685–722
- Knoche S, Vella D, Aumaitre E, Degen P, Rehage H, Cicuta P, Kierfeld J (2013) Elastometry of deflated capsules: elastic moduli from shape and wrinkle analysis. *Langmuir* 29(40):12463–12471
- Kotula AP, Anna SL (2015) Regular perturbation analysis of small amplitude oscillatory dilatation of an interface in a capillary pressure tensiometer. *J Rheol* 59(1):85–117
- Loewenberg M, Hinch EJ (1997) Collision of two deformable drops in shear flow. *J Fluid Mech* 338:299–315
- Pozrikidis C (1992) *Boundary integral and singularity methods for linearized viscous flow*. Cambridge University Press, Cambridge
- Rosen MJ (2004) *Surfactants and interfacial phenomena*. John Wiley & Sons Inc., Hoboken, New Jersey
- Sagis LMC (2011) Dynamic properties of interfaces in soft matter: experiments and theory. *Rev Mod Phys* 83(4):1367–1403
- Scriven LE (1960) Dynamics of a fluid interface. *Chem Eng Sci* 12(2):98–108
- Verwijlen T (2013) *Controlling the dynamics of liquid interfaces*. PhD thesis, Katholieke Universiteit Leuven
- Verwijlen T, Imperiali L, Vermant J (2014) Separating viscoelastic and compressibility contributions in pressure-area isotherm measurements. *Adv Colloid Interf Sci* 206:428–436

- Weatherburn CE (1955) *Differential geometry of three dimensions*. Cambridge University Press, Cambridge
- Yeow YL, Pepperell CJ, Sabturani FM, Leong YK (2008) Obtaining surface tension from pendant drop volume and radius of curvature at the apex. *Colloids Surf A Physicochem Eng Asp* 315(1):136–146
- Yunker PJ, Gratale M, Lohr MA, Still T, Lubensky TC, Yodh AG (2012) Influence of particle shape on bending rigidity of colloidal monolayer membranes and particle deposition during droplet evaporation in confined geometries. *Phys Rev Lett* 108(22):228–303
- Zinchenko AZ, Davis RH (2006) A boundary-integral study of a drop squeezing through interparticle constrictions. *J Fluid Mech* 564:227–266
- Zinchenko AZ, Rother MA, Davis RH (1997) A novel boundary-integral algorithm for viscous interaction of deformable drops. *Phys Fluids* 9(6):1493–1511